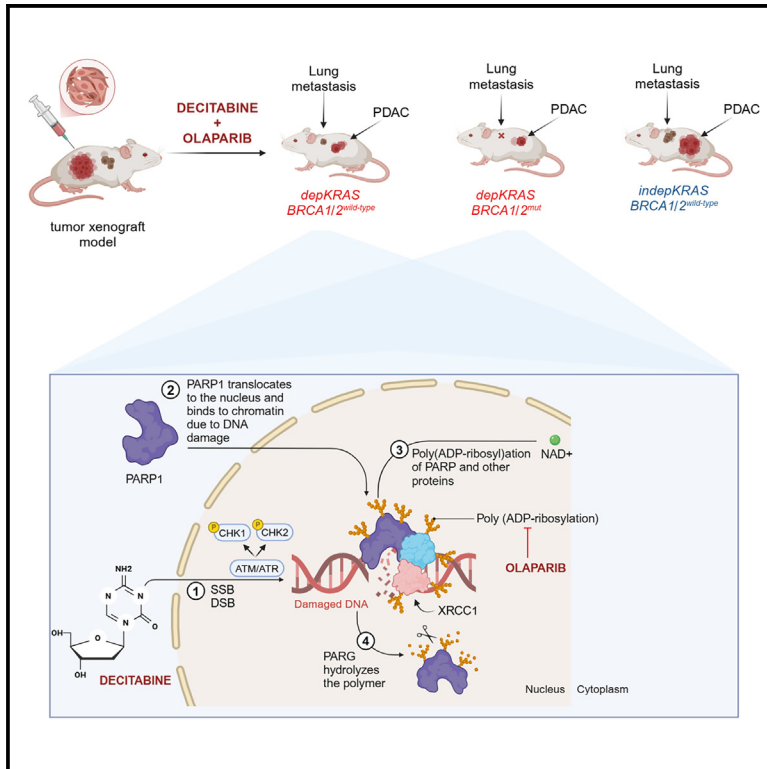


# Enhancing PDAC therapy: Decitabine-olaparib synergy targets KRAS-dependent tumors

## Graphical abstract



## Authors

Giorgia Anastasio, Michela Felaco, Alessia Lamolinara, ..., Francesca Di Modugno, Manuela Iezzi, Luca Cardone

## Correspondence

m.iezzi@unich.it (M.I.),  
luca.cardone@cnr.it (L.C.)

## In brief

Pharmacology; Cancer

## Highlights

- Decitabine (DEC) induces DNA damage in PDAC cells dependent on KRAS (dKRAS).
- PARP1 activity mediates DNA repair following DEC treatment in dKRAS-PDAC
- DEC+Olaparib synergistically targets dKRAS-PDAC, independent of BRCA mutation status
- Low-dose DEC+OLA offers reduced toxicity with strong antitumor and antimetastatic effects



## Article

# Enhancing PDAC therapy: Decitabine-olaparib synergy targets KRAS-dependent tumors

Giorgia Anastasio,<sup>1,7</sup> Michela Felaco,<sup>1,2,7</sup> Alessia Lamolinara,<sup>3,4</sup> Francesco del Pizzo,<sup>3,4</sup> Elisa Cacciagrano,<sup>3,4</sup> Carla Mottini,<sup>5</sup> Margherita Mutarelli,<sup>6</sup> Francesca Di Modugno,<sup>2</sup> Manuela Iezzi,<sup>3,4,\*</sup> and Luca Cardone<sup>1,2,8,\*</sup>

<sup>1</sup>Institute of Biochemistry and Cellular Biology, National Research Council, Monterotondo-Scalo, 00015 Rome, Italy

<sup>2</sup>Unit of Tumor Immunology and Immunotherapy, IRCCS Regina Elena National Cancer Institute, 00144 Rome, Italy

<sup>3</sup>Center for Advanced Studies and Technology, 66100 Chieti, Italy

<sup>4</sup>Department of Neurosciences, Imaging and Clinical Sciences, G. d'Annunzio University of Chieti-Pescara, 66100 Chieti, Italy

<sup>5</sup>UOSD SAFU Translational Research Area, IRCCS Regina Elena National Cancer Institute, 00144 Rome, Italy

<sup>6</sup>Institute of Applied Sciences and Intelligent Systems, National Research Council, 80078 Naples, Italy

<sup>7</sup>These authors contributed equally

<sup>8</sup>Lead contact

\*Correspondence: [m.iezzi@unich.it](mailto:m.iezzi@unich.it) (M.I.), [luca.cardone@cnr.it](mailto:luca.cardone@cnr.it) (L.C.)

<https://doi.org/10.1016/j.isci.2025.111842>

## SUMMARY

Pancreatic ductal adenocarcinoma (PDAC) shows limited response to chemotherapy, partly due to the absence of effective biomarkers for personalized treatment. Kirsten rat sarcoma viral oncogene homolog (KRAS) mutations are found in 90% of PDAC cases, and tumors dependent on KRAS (dKRAS) can be identified using gene expression signature scores. Previous research indicates that dKRAS-PDAC cells are sensitive to decitabine (DEC), an FDA-approved drug for hematological cancers, though its use in solid tumors is limited by side effects. We discovered that low-dose DEC combined with the poly (ADP-ribose) polymerase (PARP) inhibitor olaparib (OLA) enhances antitumor activity in dKRAS-PDAC. DEC induces DNA damage and activates the ataxia telangiectasia (ATR)/ataxia telangiectasia mutated (ATM)-mediated DNA damage response (DDR), with PARP1-mediated repair playing a key role. Inhibiting PARP with OLA further improves efficacy, even in BRCA1/2-wild-type and homologous recombination (HR)-proficient tumors but not in KRAS-independent tumors. The combination was especially effective in dKRAS-PDAC with a BRCA2 mutation, preventing metastasis growth. Our results support the clinical evaluation of DEC+OLA in PDAC.

## INTRODUCTION

With a 5-year survival rate of only 8%, pancreatic ductal adenocarcinoma (PDAC) is the fourth leading cause of cancer death worldwide.<sup>1</sup> Despite extensive efforts, there has been limited improvement in the therapeutic and clinical management of advanced and metastatic PDAC, as chemoresistance and tumor recurrence rates remain high. Reliable diagnostic markers for personalized therapy are still unavailable, resulting in treatments being administered without stratifying patients for optimal benefits and likelihood of response.

Between 90 and 95% of PDAC cases harbor a Kirsten rat sarcoma viral oncogene homolog (KRAS) oncogene-activating mutation.<sup>2</sup> Genetically modified mouse models have demonstrated the essential role of KRAS-dependent signaling in PDAC growth and development.<sup>3</sup> By investigating KRAS-associated gene profiles in PDAC, subtypes with a molecular dependency on KRAS (dKRAS) can be identified, referring to tumors whose growth still requires active KRAS-dependent signaling.<sup>4,5</sup> The extent of KRAS dependency can differ even with a similar genomic KRAS mutation,<sup>4,5</sup> indicating that KRAS mutations might have limited predictive value regarding tumor cells' reliance on

KRAS-dependent pathways. Computational gene signature-based scores can stratify tumors, cancer cell lines, and patient-derived xenografts (PDXs) to predict tumor cell dependence on KRAS (dKRAS) in PDAC.<sup>4</sup> A significant proportion of PDAC cases fall under the dKRAS subtype.<sup>4</sup> Consequently, transcriptional scores of KRAS activation and dependency can be effectively exploited as biomarkers for tumor classification in PDAC.

Drug repurposing, the use of FDA-approved medicines for new therapeutic indications, is a novel approach to redirecting therapies in cancer.<sup>6,7</sup> Decitabine (5-Aza-2-deoxycytidine, DEC) is approved to treat myelodysplastic syndromes and acute myeloid leukemia. Its anticancer activity has been considered in other clinical settings, with more than fifty clinical trials testing the repurposing of DEC alone or in combination with chemotherapies or immunotherapies for treating solid tumors, including breast, ovarian, colon, lung, pancreatic cancers, and sarcoma (<https://clinicaltrials.gov/>).<sup>8</sup> However, DEC treatment is associated with severe hematological toxicity in approximately 30% of cases, including G3/4 febrile neutropenia. These adverse events may limit treatment efficacy and adversely affect the quality of life for patients, particularly with high-dose



administration.<sup>9</sup> This underscores the importance of identifying therapeutic strategies to mitigate DEC side effects while preserving its anticancer efficacy. Enhancing our understanding of DEC's mode of action and identifying biomarkers that predict patient response to DEC is crucial for its successful clinical repurposing in solid tumors.

DEC, an irreversible inhibitor of DNA methyltransferase and a cytosine analog incorporated into DNA during replication, has been extensively studied for its anticancer activity as a DNA-demethylating agent.<sup>10</sup> This activity results in gene expression modulation, specifically reactivation of antiapoptotic genes<sup>11</sup> enhancing immune-checkpoint inhibitor therapy by overexpressing mutated neoantigens,<sup>12</sup> or reverting T cell exhaustion.<sup>13</sup> We previously demonstrated that DEC exhibited potent antitumor and antimetastatic properties in the KRAS-dependent PDAC subtype, although the mechanism remains unclear. In dKRAS- but not in KRAS-independent PDAC, DEC treatment induced cell-cycle arrest at the G2/M phase and induced phospho-H2AX, a DNA damage response (DDR) marker,<sup>7</sup> suggesting that, in dKRAS-PDAC, DEC might induce DNA damage. Research findings have shown that DEC can induce a DNA damage response mediated by the ataxia telangiectasia mutated (ATM) protein and lead to double-strand breaks (DSBs) in HeLa cells, colon cancer cells,<sup>14</sup> and multiple myeloma cells.<sup>15</sup> Moreover, acute myeloid leukemia (AML) cells deficient in base excision repair (BER) were hypersensitive to DEC, and BER was required to remove aberrant bases from DNA and recognize abasic sites generated by DEC,<sup>16</sup> and DEC also induced mitotic stress in AML cells.<sup>17</sup> Thus, the available evidence suggests that DEC's mechanism of action as an antitumor agent might also involve DDR.

The poly (ADP-ribose) polymerase (PARP) plays a key role in DDR to maintain genomic integrity in highly replicative cells.<sup>18</sup> PARP inhibitors (PARPi) have demonstrated clinical efficacy against several solid tumor types carrying BRCA1/2 genomic mutations and homologous recombination deficiency (HRD), through a synthetic lethal-based mechanism.<sup>19,20</sup> In PDAC, the PARPi olaparib (OLA) has been approved as maintenance therapy in platinum-treated tumors carrying BRCA1/2 mutations. More than forty clinical trials are testing the efficacy of PARPi alone or in combination with other treatments at various stages of PDAC. There is also growing interest in investigating the clinical efficacy of PARPi in solid tumors regardless of BRCA1/2 mutations, based on functional deficits in BRCA (BRCAness), microsatellite instability (MSI), or defects in the DNA homologous recombination repair (HRR) pathway. Genomic mutational profiles of HR-related genes are under investigation as biomarkers of response.<sup>21</sup> Additionally, molecular surrogate readouts of HRD can identify a greater proportion of patients with HRD than analyses limited to gene-level approaches.<sup>21,22</sup> Evidence in breast and ovarian cancers has demonstrated that a RAD51 score, estimated as the percentage of geminin-positive cells carrying RAD51-positive nuclear foci, might predict tumor cellular HR status. RAD51 scores are very low in HR-deficient cells and correlate with responses to PARPi or platinum treatments.<sup>23</sup> Thus, extending the population who might benefit from PARPi beyond the available biomarkers, which is also the focus of the present manuscript,

could significantly enhance clinical practice and treatment options for PDAC patients.

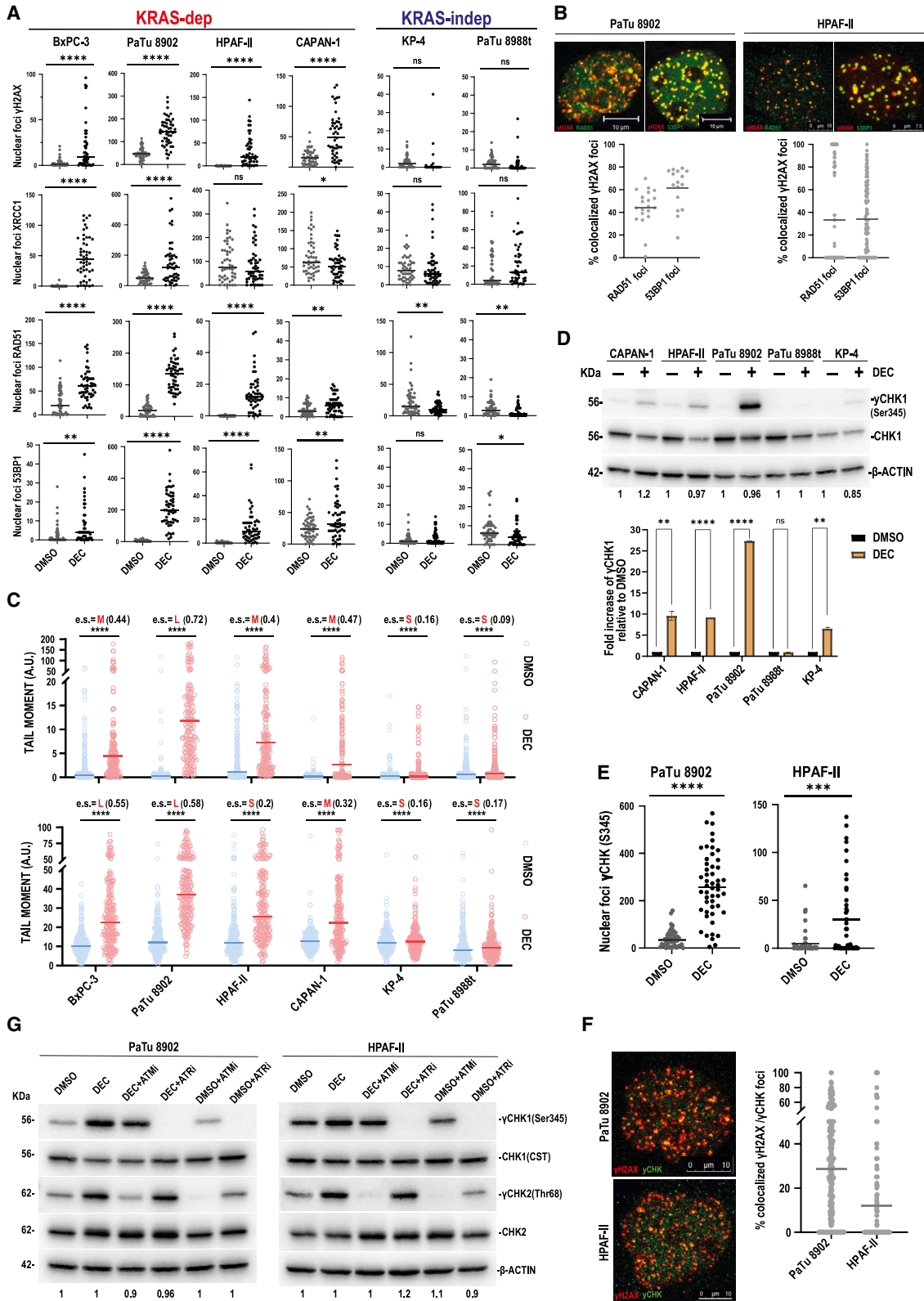
Previous studies have demonstrated molecular crosstalk between PARP activity and DEC. OLA has been demonstrated to block DEC-induced BER replication fork collapse, thereby inducing double-strand breaks and cell death, and promoting synthetic lethality in AML.<sup>16</sup> Further research has reported increased cytotoxic effects of combining PARP inhibitors with DNA demethylating agents in AML subtypes and BRCA wild-type breast cancer cells,<sup>24</sup> particularly in combination with irradiation. Based on this evidence, we speculated that PARP activity is involved in the repair process following DEC-induced DNA damage in KRAS-dependent PDAC (dKRAS-PDAC), potentially providing a therapeutic window for a synergistic drug combination of DEC with PARP inhibitors such as OLA. We investigated the preclinical efficacy of the combination of DEC and OLA in the dKRAS-PDAC subtype identified using transcriptional-based scores for KRAS dependency.

## RESULTS

### DEC induces robust DNA damage and DDR activation in KRAS-dependent PDAC cells through ATM/ATR-mediated pathways

PDAC cellular models from the Cancer Cell Line Encyclopedia (CCLE) panel can be classified based on transcriptomic assessments of their similarity to reference gene signatures of KRAS dependency and activation (referred to as the S- and L-scores, respectively), previously validated (Figure S1; Table S1). To elucidate the mode of action of DEC in PDAC, we investigated the activation of DDR markers associated with single-strand breaks (SSBs) and DSBs. This included examining XRCC1-positive nuclear foci for SSBs and 53BP1- and RAD51-positive nuclear foci for DSBs. We selected dKRAS-PDAC cell lines, such as BxPC-3, PaTu 8902, HPAF-II, and CAPAN-1 based on their high KRAS dependency scores (both L- and S-scores) (Figure S1; Table S1). Quantification of immunofluorescence images showed a strong and statistically significant induction of phospho-Ser139( $\gamma$ )H2AX-, XRCC1-, RAD51-, and 53BP1-positive nuclear foci in dKRAS-PDAC cells following 72 h of DEC treatment. In contrast, the analysis of KRAS-independent (indepKRAS) cell lines, those with low transcriptional scores for KRAS dependency and activation (Figure S1; Table S1), such as PaTu 8988t and KP-4, did not show any significant increase in number of nuclear foci for these markers following DEC treatment (Figures 1A and S3). Furthermore,  $\gamma$ H2AX-positive foci induced by DEC in dKRAS-PDAC cells colocalized with RAD51- and 53BP1-positive foci (Figure 1B).

We further investigated the extent of DNA damage using the comet assay. The comet assay revealed that the tail moment (TM) value, indicative of DNA fragmentation following DNA breaks, was statistically increased in dKRAS-PDAC cells (PaTu 8902, BxPC-3, HPAF-II, and CAPAN-1) following DEC treatment. The effect size for DEC versus DMSO treatment in dKRAS-PDAC cells was calculated to be medium to large, indicating a robust induction of DNA damage (Figure 1C). Conversely, the indepKRAS-PDAC cell lines (PaTu 8988t and KP-4) showed very low or no significant increase in TM values following DEC treatment,



(legend on next page)

with effect sizes calculated to be small (Figure 1C). This differential response underscores the specificity of DEC-induced DNA damage in KRAS-dependent versus KRAS-independent PDAC cells. A significant increase in TM following DEC treatment was observed using both alkaline and neutral comet assay methods, confirming that DEC induces both SSB and DSB DNA damage, as indicated by DDR marker analysis.

Next, we examined the activation of specific DNA damage protein checkpoints. Immunoblot analysis demonstrated that DEC induced the phosphorylation of checkpoint kinase 1 (CHK1) at residue Ser345 in dKRAS-PDAC cell lines, a key residue for kinase activation following DNA damage (Figure 1D). Accordingly, nuclear phospho-Ser345( $\gamma$ )CHK1-positive foci were detected in dKRAS-PDAC cell models following DEC treatment (Figure 1E), with  $\gamma$ CHK1-positive nuclear foci demonstrating colocalization with  $\gamma$ H2AX-positive foci (Figure 1F). Inhibiting ATR (ataxia telangiectasia and Rad3-related), the key kinase responsible for CHK1 phosphorylation and activation, using the specific ATR inhibitor (ATRi) BAY-1895344, completely suppressed DEC-induced phosphorylation of  $\gamma$ CHK1 (Figures 1G and S4A). Furthermore, the specific ATM in-

hibitor (ATMi) AZD1390 completely inhibited DEC-induced phosphorylation at the phospho-Ser68( $\gamma$ )CHK2 target residue and reduced the extent of DEC-induced CHK1 phosphorylation (Figures 1G and S4B). Overall, these data demonstrate that DEC induces robust DNA damage and DDR in dKRAS-PDAC cells, while indepKRAS cells remain insensitive. The DDR involves ATM/ATR-mediated DNA damage checkpoints through the activation of CHK1 and CHK2 kinases, resulting from the accumulation of both SSB and DSB DNA damage.

### PARP1 activity via PARylation mediates DNA repair and DDR following DEC treatment

Based on the role of PARP1 and PARP activity in both SSB and DSB DNA repair<sup>18,19</sup> and the previously reported crosstalk with DEC activity,<sup>16,24</sup> we next investigated the role of PARP1 activation following DEC treatment in dKRAS- and indepKRAS-PDAC cells. Immunoblot analysis of PARP1 extracted from nuclear protein fractions demonstrated that a nanomolar concentration (100 nM) of DEC induced the selective accumulation of PARP1 in the nuclear insoluble (NI), chromatin-bound protein fraction (Figure 2A, upper panels), but not in the nuclear soluble

### Figure 1. DEC induces robust DNA damage and DDR activation in KRAS-dependent PDAC cells through ATM/ATR-mediated pathways

(A) Quantification of immunofluorescence analysis of phospho-( $\gamma$ )H2AX(Ser139)-, XRCC1-, RAD51-, and 53BP1-positive nuclear foci in dKRAS-PDAC cell lines (BxPC-3, PaTu 8902, HPAF-II, and CAPAN-1) and indepKRAS-PDAC cell lines (PaTu 8988t and KP-4) following DMSO (vehicle) or DEC (1.25  $\mu$ M) treatment for 72 h. Data are presented as median from a representative replicate experiment. At least 50 nuclei were counted for each replicate using immunofluorescence analysis with CellProfiler 4.2.1.

Statistical analysis was performed using GraphPad Prism. Statistical significance for DMSO vs. DEC-treated cells was calculated using the unpaired two-tailed Student's t test: \* $p < 0.05$ , \*\* $p < 0.01$ , \*\*\* $p < 0.001$ , \*\*\*\* $p < 0.0001$ , ns:  $p > 0.05$ . For representative images of the experiment, please see Figure S3.

(B) Colocalization analysis of  $\gamma$ H2AX with RAD51- and 53BP1-positive nuclear foci in dKRAS-PDAC cells following DEC (1.25  $\mu$ M) treatment for 72 h. Upper panels: representative images of confocal microscopy analysis of PaTu 8902 and HPAF-II co-stained for  $\gamma$ H2AX with RAD51 or 53BP1. The nuclei were counterstained with DAPI. Scale bar, 10  $\mu$ m. Magnification,  $\times 60$ . Lower panels: Dot plots representative of the percentage of colocalized foci. Data are presented as median from a representative replicate experiment. From 20 to 100 nuclei were counted for each replicate using immunofluorescence analysis with CellProfiler 4.2.1. Data analysis was performed using GraphPad Prism.

(C) Quantification of comet tail moment (TM), which measures DNA fragmentation, in dKRAS-PDAC cells (PaTu 8902, BxPC-3, HPAF-II, and CAPAN-1) and indepKRAS-PDAC cells (PaTu 8988t and KP-4) following treatment with DMSO (vehicle) or DEC (1.25  $\mu$ M) for 72 h. Data are presented as median from a representative replicate experiment. At least 200 nuclei were counted for each replicate. Alkaline (upper panel) and neutral (lower panel) comet assays were performed. To quantify the magnitude of DEC-induced DNA damage compared to DMSO, the effect size (e.s.) was estimated by the Wilcoxon test from three to six biological replicates. The Rstatix package was implemented for the calculation of the effect size.

Statistical significance for DMSO vs. DEC-treated cells was calculated using the Mann-Whitney test: \*\*\*\* $p < 0.0001$ . Medium (M) to large (L) effect sizes suggest substantial DNA damage, while small (S) effect sizes indicate minimal to no response to DEC treatment. The effect sizes for DEC vs. DMSO treatments were calculated as follows: BxPC-3 (alkaline: M; neutral: L), PaTu 8902 (alkaline: L; neutral: L), HPAF-II (alkaline: M; neutral: S), and CAPAN-1 (alkaline: M; neutral: M). No significant increase in TM was observed in indepKRAS cells, with effect sizes calculated as Small (S). Alkaline and neutral comet assays confirmed significant DNA fragmentation indicative of single-strand breaks (SSBs) and double-strand breaks (DSBs) in dKRAS-PDAC cells following DEC treatment.

(D) Upper panel: representative immunoblots showing phosphorylation of CHK1 at Ser345 in the indicated cell lines following DEC (1.25  $\mu$ M) treatment for 72 h. Equal amounts of total protein extracts were analyzed with the indicated antibodies. Immunoblot for actin was used as a loading control. Numbers below the actin immunoblots represent the ratio of actin densitometry of each sample relative to DMSO. Lower panel: Histograms represent the quantification of  $\gamma$ CHK1(Ser345)/CHK1 densitometry. Histograms represent mean  $\pm$  SD (represented by error bars) from triplicate experiments.

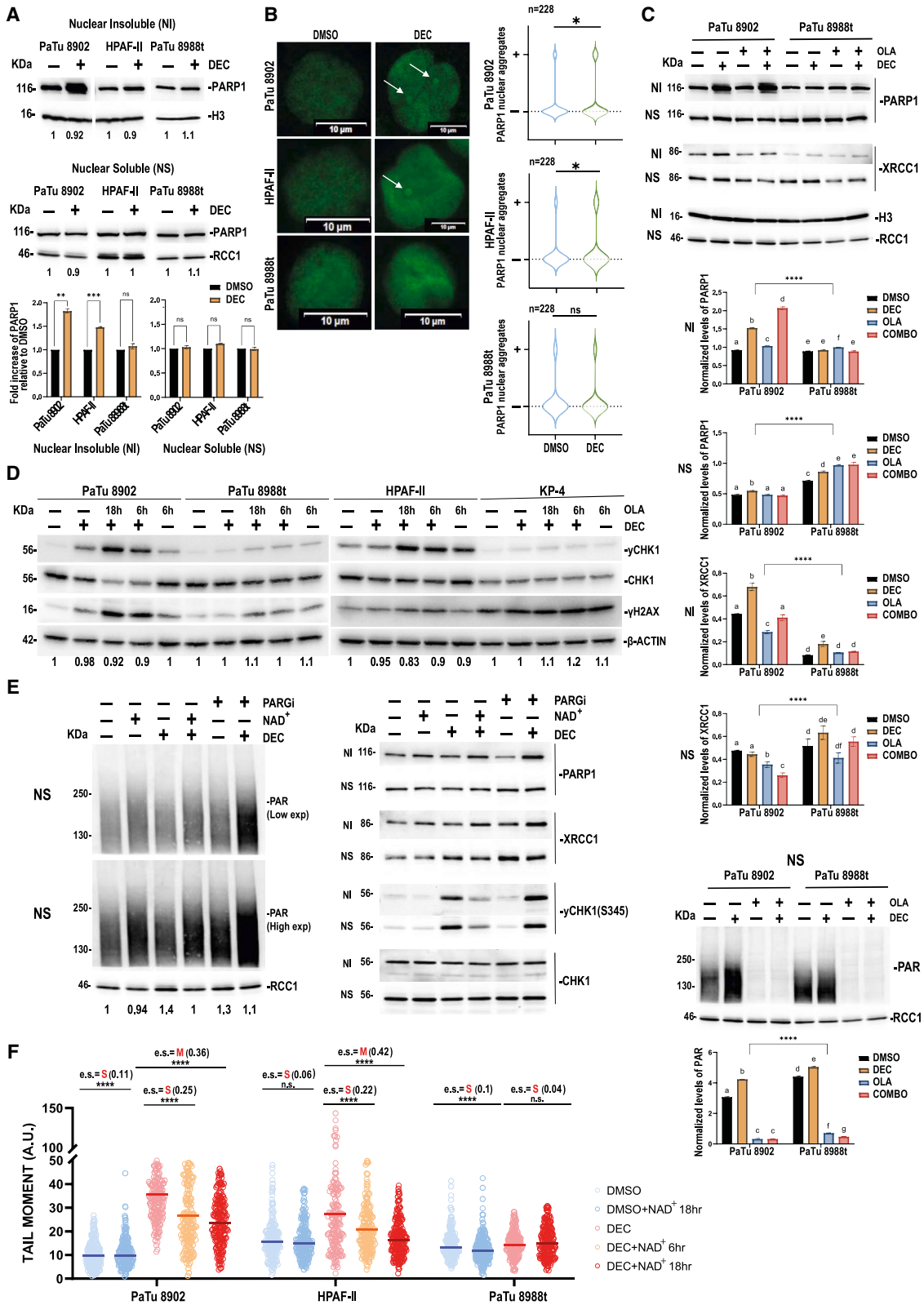
Statistical significance for DMSO vs. DEC-treated cells was calculated using an unpaired t test: \*\* $p < 0.01$ , \*\*\*\* $p < 0.0001$ , ns:  $p > 0.05$ ; statistical analysis was performed using GraphPad Prism.

(E) Quantification of immunofluorescence analysis of nuclear  $\gamma$ CHK1(Ser345) positive foci in dKRAS-PDAC cell models following DEC treatment. Data are presented as median from a representative replicate experiment. At least 50 nuclei were counted for each replicate by image analysis with CellProfiler 4.2.1. Statistical analysis was performed using GraphPad Prism.

Statistical significance for DMSO vs. DEC-treated cells was calculated using an unpaired t test: \*\*\* $p < 0.001$ , \*\*\*\* $p < 0.0001$ .

(F) Colocalization analysis of  $\gamma$ H2AX with  $\gamma$ CHK1-positive nuclear foci in dKRAS-PDAC cells following DEC (1.25  $\mu$ M) treatment for 72 h. Left panel: representative images of confocal microscopy analysis of PaTu 8902 and HPAF-II co-stained for  $\gamma$ H2AX and with  $\gamma$ CHK1. Scale bars, 10  $\mu$ m. Magnification,  $\times 60$ . Right panel: Dot plots representative of the percentage of colocalized foci. Data are presented as median from a representative replicate experiment. From 20 to 100 nuclei were counted for each replicate by image analysis with CellProfiler 4.2.1. Data analysis was performed using GraphPad Prism.

(G) ATR or ATM inhibitors suppress DEC-induced phosphorylation of CHK1 at Ser345 and CHK2 phosphorylation at Thr68 in dKRAS-PDAC cells (PaTu 8902 and HPAF-II). Representative immunoblots of total proteins extracted from indicated cell lines treated with DMSO or DEC (100 nM) for 72 h. Where indicated, the ATM inhibitor (ATMi) AZD1390 (10 nM) or the ATR inhibitor (ATRi) BAY-1895344 (2  $\mu$ M) was added 1 h before harvesting cells. Equal amounts of total protein extracts were analyzed with the indicated antibodies. Immunoblot for actin was used as a loading control. Numbers below the actin immunoblot represent the ratio of actin densitometry of each sample relative to DMSO in each cell line. Quantifications of  $\gamma$ CHK1/totalCHK1 and  $\gamma$ CHK2/CHK2 are reported in Figure S4.



(legend on next page)

(NS), high-salt extracted protein fraction (Figure 2A, lower panels) in dKRAS-PDAC cells (PaTu 8902 and HPAF-II) but not in indepKRAS cells (PaTu 8988t). DEC increased the number PARP1 nuclear foci and aggregates as revealed by immunofluorescence analysis (Figure 2B) in dKRAS-PDAC cells (PaTu 8902 and HPAF-II) but not in indepKRAS cells (PaTu 8988t).

To address the mechanistic role of PARP1 and PARP activity in response to DEC in PDAC, we first monitored molecular effects following acute PARP activity inhibition using the FDA-approved PARP inhibitor olaparib (OLA) in cells pre-treated for 72 h with a nanomolar concentration of DEC (100 nM). Adding

OLA alone for 18 h before harvesting cells further increased PARP1 accumulation in the nuclear insoluble (NI), chromatin-bound fraction in DEC-treated PaTu 8902 cells. Drug treatments did not increase levels of PARP1 in the nuclear soluble (NS), high-salt extracted protein fraction (Figure 2C). In contrast, in indepKRAS cells (PaTu 8988t), we did not observe accumulation of PARP1 in the NI protein fraction. Since PARylation of PARP1 is known to recruit repair effectors such as XRCC1 to the damaged site for repair, we monitored the amount of XRCC1 in the nuclear fractions. Indeed, DEC treatment increased the amount of XRCC1 in NI fraction in PaTu 8902 cells. Treatment with OLA was sufficient to fully inhibit DEC-induced XRCC1

### Figure 2. PARP1 activity via PARylation mediates DNA repair and DDR following DEC treatment

(A) Immunoblot analysis of PARP1 in nuclear protein fractions extracted from dKRAS-PDAC cells (PaTu 8902 and HPAF-II) and indepKRAS-PDAC cells (PaTu 8988t) treated with DMSO (vehicle) or decitabine (DEC) at 100 nM for 72 h. Upper panels show PARP1 accumulation in the chromatin-bound, nuclear insoluble (NI) fraction from dKRAS cells but not from indepKRAS cells. The middle panels display PARP1 levels in the high-salt extracted, nuclear soluble (NS) protein fraction, where no significant changes were observed. Lower panels: Histograms represent the quantification of the PARP1 protein amount over Histone H3 protein used as a loading control for the NI fraction or over RCC1 protein used as a loading control for the NS fraction. Histograms represent mean  $\pm$  SD from triplicate experiments.

Statistical significance for DMSO vs. DEC-treated cells was calculated using an unpaired t test: \*\* $p < 0.01$ , \*\*\* $p < 0.001$ , ns:  $p > 0.05$ .

(B) Left panels: representative immunofluorescence images of PARP1 nuclear staining in dKRAS-PDAC cells (PaTu 8902 and HPAF-II) and indepKRAS-PDAC cells (PaTu 8988t) following treatment with DMSO (vehicle) or decitabine (DEC) at 100 nM for 72 h. Arrows indicate DEC-induced PARP1 protein aggregates (dots) in the nucleus. The nuclei were counterstained with DAPI. Scale bars, 10  $\mu$ m. Magnification,  $\times 60$ . Right panels: Quantification of PARP1-positive nuclear aggregates as presented in the left panels in dKRAS-PDAC cells (PaTu 8902 and HPAF-II) and indepKRAS-PDAC cells (PaTu 8988t). "+" indicates positive cells presenting at least one PARP1 positive aggregate signal. "-" indicates negative cells, showing no nuclear aggregates of PARP1. Data are presented as mean from a representative replicate experiment. The indicated nuclei (n) were counted for each replicate by image analysis with CellProfiler 4.2.1. Data analysis was performed using GraphPad Prism.

Statistical significance for the mean difference of DEC-treated cells vs. DMSO-treated cells was determined using the unpaired two-tailed Student's t test. \* $p < 0.05$ ; ns:  $p > 0.05$ .

(C) PARylation promotes DEC-induced recruitment of XRCC1 on the chromatin-bound protein fraction. Upper panels: representative images of immunoblot analysis for PARP1 and XRCC1 in nuclear protein fractions from dKRAS-PDAC cells (PaTu 8902) and indepKRAS-PDAC cells (PaTu 8988t) treated for 72 h with DMSO, DEC (100 nM), OLA (1.4  $\mu$ M), or DEC combined with OLA. OLA was added 18 h before harvesting cells. NI: nuclear insoluble, chromatin-bound protein fraction; NS: nuclear soluble, high-salt extracted protein fraction. Middle panels: histograms represent the quantification of XRCC1 and PARP1 protein over H3 immunoblot used as loading control for the NI fraction or over RCC1 protein used as loading control for the NS fraction. Histograms represent mean  $\pm$  SD (represented by error bars) from triplicate experiments. Statistical analyses were performed using GraphPad Prism 8 and R with a two-way ANOVA test between pairs of cell lines and One-way ANOVA with multiple comparisons through post-hoc Tukey HSD (honestly significant difference) test within experimental set of each cell line (same letter in the graph represents no statistical relevance in the difference between groups, different letter represents a significant  $p$  value ( $< 0.05$ ) of the comparison between groups). Lower panel: representative images of immunoblot analysis for PAR (PARylated proteins) in the NS protein fraction, showing the effective inhibition of PARP activity by OLA under the indicated experimental conditions. Histograms represent mean  $\pm$  SD (represented by error bars) from triplicate experiments. Statistical analyses were performed as above described.

(D) Activation of DDR markers was significantly enhanced by combined DEC and OLA treatment in dKRAS cells but not in indepKRAS PDAC cells. Immunoblot analysis of  $\gamma$ CHK1(Ser 345) and  $\gamma$ H2AX(Ser139) in dKRAS-PDAC cells (PaTu 8902 and HPAF-II) and indepKRAS-PDAC cells (PaTu 8988t and KP-4) treated for 72 h with DMSO, DEC (100 nM), OLA, or DEC combined with OLA. OLA was added for the indicated time before harvesting cells and used as follows: 1.4  $\mu$ M for 18 h; 5  $\mu$ M for 6 h. Immunoblot for actin was used as a loading control. Numbers below the actin immunoblots represent the ratio of actin densitometry of each sample relative to DMSO. The quantifications of  $\gamma$ CHK1 and  $\gamma$ H2AX are reported in Figure S5A.

(E) Left panels: enhancing PARP1 activity by Nicotinamide adenine dinucleotide (NAD<sup>+</sup>) supplementation. dKRAS-PDAC cells (PaTu 8902) were treated with DMSO or DEC (100 nM) for 72 h and supplemented with NAD<sup>+</sup> (0.5 mM) for 3 h before harvesting the cells. Immunoblot analysis (low and high exposures) of the nuclear soluble protein fraction showed increased protein PARylation, indicating enhanced PARP activity following NAD<sup>+</sup> supplementation. As a positive control, the poly(ADP ribose) glycohydrolase (PARG) inhibitor PDD00017273 (1  $\mu$ M) was added 1 h before harvesting cells. Adding PARGi resulted in the accumulation of PARylated proteins. Quantifications of immunoblots are reported in Figure S5B. Right panels: enhancing PARP1 activity by NAD<sup>+</sup> supplementation in DEC-treated cells increased the amount of chromatin-bound, nuclear insoluble PARP1 and XRCC1, and reduced the extent of DEC-induced  $\gamma$ CHK1. Left panels: representative images of immunoblot analysis for PARP1, XRCC1,  $\gamma$ CHK1, and CHK1 in nuclear fractions from experiments performed as in (E). NI: nuclear insoluble, chromatin-bound fraction; NS: nuclear soluble, high-salt extracted protein fraction. Quantifications of immunoblots are reported in Figures S5C–S5E.

(F) Enhancing PARP1 activity by NAD<sup>+</sup> supplementation significantly reduced DEC-induced DNA fragmentation in dKRAS cells, indicating enhanced DNA repair by PARylation. Quantification of comet tail moment (TM) values from neutral comet assays of dKRAS-PDAC cells (PaTu 8902 and HPAF-II) and indepKRAS-PDAC cells (PaTu 8988t) treated with DMSO, DEC (100 nM), and supplemented, where indicated, with NAD<sup>+</sup> (0.5 mM) for 6 or 18 h before harvesting the cells for comet assays. Data are presented as median from a representative replicate experiment. At least 200 nuclei were counted for each replicate. To quantify the magnitude of treatment-induced DNA damage among groups, the effect size (e.s.) was estimated by the Wilcoxon test by three to seven biological replicates. The Rstatix package was implemented for the calculation of the effect size. Statistical significance among the indicated comparison groups was calculated using the Dunn's test. Statistical significance: \*\*\*\*,  $p < 0.0001$ . Medium (M) to large (L) effect sizes suggest substantial DNA damage, while Small (S) effect sizes indicate minimal to no response to treatment. Effect sizes (e.s.): S = small; M = medium; L = large. The calculated effect sizes indicate a robust induction of DNA damage by DEC that could be in part rescued by NAD<sup>+</sup> supplementation. No significant increase in TM was observed in indepKRAS cells (PaTu 8988t) following DEC or NAD<sup>+</sup> treatments, with effect sizes calculated as small (S).

accumulation within the NI, chromatin-bound protein fraction. IndepKRAS cells (PaTu 8988t) showed a low accumulation of XRCC1 following DEC in the NI fraction, which was also inhibited by OLA treatment (Figure 2C).

To investigate the functional consequence of the inhibition of PARP activity in DEC-treated cells, we monitored the activation of DDR markers. Immunoblot analyses showed that acute treatment with OLA following DEC treatment was sufficient to enhance the activation of DDR markers such as  $\gamma$ CHK1 and  $\gamma$ H2AX in dKRAS-PDAC cells (PaTu 8902 and HPAF-II), compared to DEC or OLA treatment alone. In contrast, in indepKRAS-PDAC cells (PaTu 8988t and KP-4), DEC was ineffective, and adding OLA did not enhance the extent of DDR marker activation compared to the effect of treating with OLA alone (Figures 2D and S5A).

We next tested the effects of promoting PARP activity. To this aim, we supplemented DEC-treated cells with nicotinamide adenine dinucleotide ( $\text{NAD}^+$ ), a cofactor necessary for PARP enzymatic activity. The supplementation of  $\text{NAD}^+$  was effective in increasing PARP1 activity, as measured by the specific analysis of total protein PARylation by immunoblot (Figure 2E, left panels; Figure S5B). This effect was mirrored by treating cells with the poly (ADP-ribose) glycohydrolase inhibitor (PARGi) (PDD00017273), which, by inhibiting the de-PARylation of PARylated proteins, served as a positive control for detecting protein PARylation enhancement. Immunoblot studies demonstrated that enhancing PARylation either by  $\text{NAD}^+$  or PARGi treatments was sufficient to increase the amount of PARP1 in the chromatin-bound, nuclear insoluble (NI) protein fraction, but not in the soluble nuclear fraction, following DEC treatment (Figure 2E, right panels; Figure S5C). These results were consistent with the well-established role of PARP1 PARylation in stabilizing PARP1 recruitment on damaged chromatin to recruit DNA repair complexes. Accordingly, in DEC-treated cells,  $\text{NAD}^+$  supplementation also increased the amount of XRCC1 in the chromatin-bound fraction resulting in a parallel reduction of XRCC1 protein amount in the soluble nuclear fraction of DEC-treated cells (Figure 2E, right panels; Figure S5D). This effect was also mirrored by the PARGi. Furthermore, the enhancement of PARP1 activity by  $\text{NAD}^+$  was sufficient to reduce the extent of DEC-induced  $\gamma$ CHK1 activation (Figure 2E, right panels; Figure S5E), indicating a reduction in the DNA damage response. Interestingly, PARGi did not reduce  $\gamma$ CHK1 levels in DEC-treated samples, suggesting persistent DNA damage. This result is expected and is well-consistent with the established role of PARylation/de-PARylation cycles of PARP1 required for proper repair mechanisms following DNA damage, where PARG activity was demonstrated to be essential to support the dynamic assembly/disassembly of multienzyme complexes on damaged DNA for repair<sup>18,25</sup>

The enhancement of PARP1 activity by  $\text{NAD}^+$  reduced the extent of  $\gamma$ CHK1 activation (Figure 2E, right panels), suggesting reduced DNA damage. To confirm this, we analyzed the extent of DEC-induced DNA damage and fragmentation using the comet assay. Indeed, the effect size analysis of the TM indicated a robust induction of DNA damage by DEC in dKRAS-PDAC cells (PaTu 8902 and HPAF-II). This damage was partially reduced by  $\text{NAD}^+$  supplementation, with a calculated effect size of moderate

(M) when comparing DEC-treated cells to DEC-treated cells supplemented with  $\text{NAD}^+$  (Figure 2F).

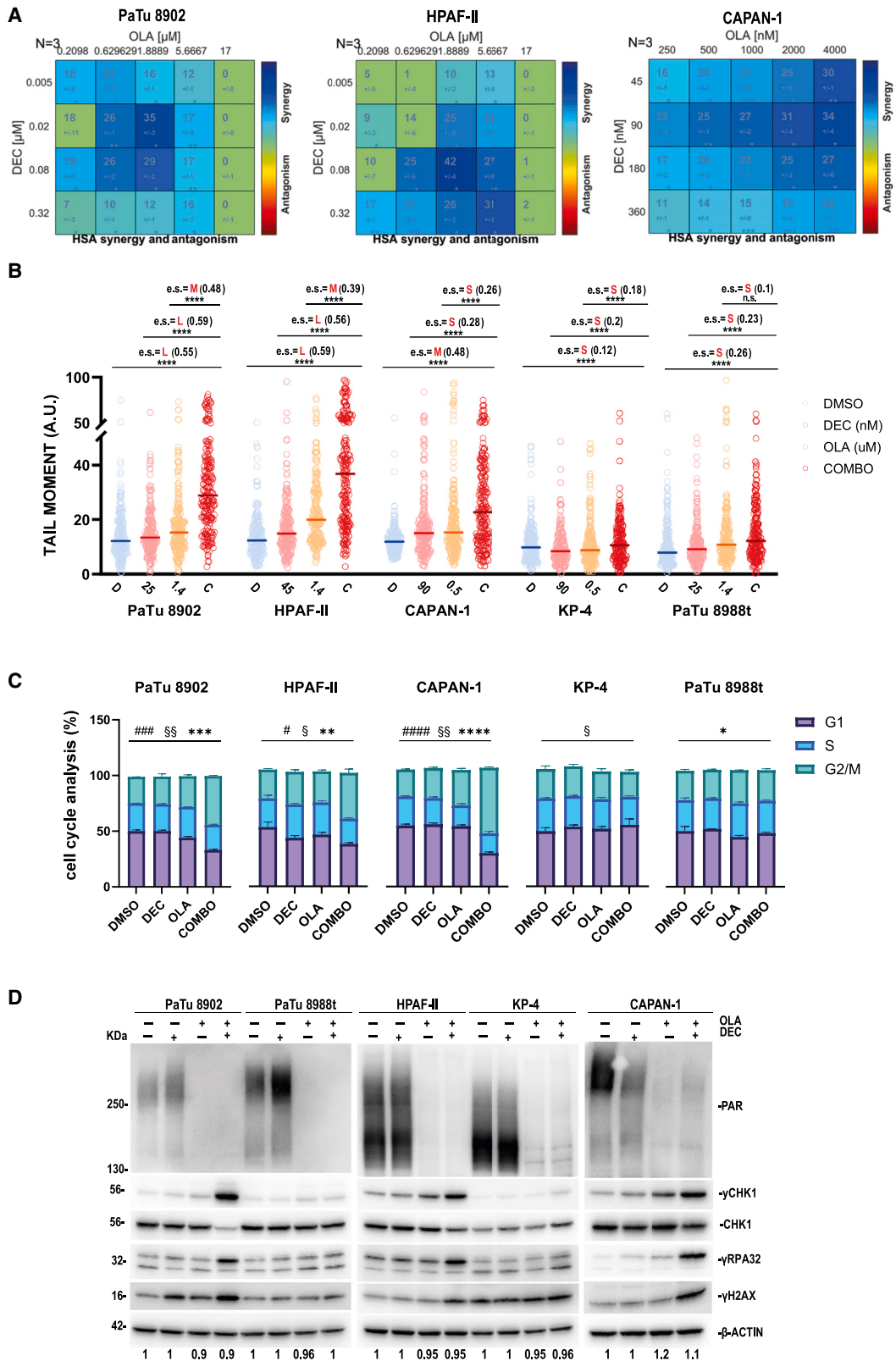
Overall, these results demonstrated that PARP1 activity played a mechanistic role in the DDR and DNA damage repair induced by DEC in KRAS-dependent PDAC. The acute inhibition of PARP activity by OLA enhances DEC-induced DNA damage, highlighting the potential for combined therapeutic strategies targeting PARP activity in KRAS-dependent PDAC.

### Synergistic combination of low-dose DEC with OLA in dKRAS-PDAC cells

The aforementioned results prompted us to investigate whether OLA might enhance the antitumor activity of DEC against dKRAS-PDAC. Due to the well-established efficacy of PARPi such as OLA in the context of *BRCA1/2* mutated tumors, we considered the effects of drug treatment in both dKRAS-/*BRCA1/2*<sup>wild-type</sup> PDAC cell lines (PaTu 8902 and HPAF-II) and dKRAS-/*BRCA2*<sup>mut</sup> PDAC cells (CAPAN-1). We utilized the Combenefit software to analyze synergy, additivity, or antagonism between the OLA and DEC drug combination in a seven-day experiment. A matrix model (HAS) of combination analysis showed that OLA and DEC were highly synergistic or additive in dKRAS-/*BRCA1/2*<sup>wild-type</sup> PDAC cell lines across the entire range of tested concentrations (Figure 3A). Notably, DEC and OLA were highly synergistic in dKRAS-/*BRCA2*<sup>mut</sup> PDAC cells (CAPAN-1) across all tested concentrations. The synergistic effect was further demonstrated through the Calcsyn method in a seven-day experiment. Figure S7 shows plots of the combination index calculated for the interaction between the two drugs. Interestingly, both models predicted that in dKRAS-/*BRCA1/2*<sup>wild-type</sup> PDAC, the effect moved from synergistic to additive when both drugs were used at higher concentration ranges, supporting the advantage of nanomolar, low-dosage drug combinations, which would be beneficial in a clinical context. Additionally, both models predicted that in dKRAS-/*BRCA2*<sup>mut</sup> PDAC cells (CAPAN-1), the combination was synergistic across all tested concentrations.

Based on combination index results, we tested the cytotoxic effects of an even lower nanomolar concentration (25 nM) of DEC in combination with OLA (hereafter referred to as "COMBO") by simultaneously co-treating cells with both drugs in functional assays *in vitro*. We first monitored the genotoxic effect of COMBO by comet assay (Figure 3B). Results demonstrated that the tail moment significantly increased in dKRAS-/*BRCA1/2*<sup>wild-type</sup> PDAC cell lines (PaTu 8902, HPAF-II) and dKRAS-/*BRCA2*<sup>mut</sup> PDAC cells (CAPAN-1) treated for 72 h with COMBO. Indeed, the calculated effect size of the tail moment in COMBO-treated cell lines was large (L) when compared to untreated cells or single-drug treatments alone. The increase in the tail moment following COMBO treatment was observed by both alkaline and neutral comet assay methods. Conversely, the indepKRAS-/*BRCA1/2*<sup>wild-type</sup> PDAC cell lines (PaTu 8988t and KP-4) showed very low or no significant increase in tail moment values following COMBO treatment, with effect sizes calculated to be small compared to the vehicle as well as to single agents alone (Figures 3B and S8).

COMBO, but not the single treatments, induced a significant G2/M-phases arrest, with a reduction in S- and G1-phases of



(legend on next page)

the cell cycle in dKRAS-/BRCA1/2<sup>wild-type</sup> PDAC cell lines (PaTu 8902 and HPAF-II) and dKRAS-/BRCA2<sup>mut</sup> PDAC cells (CAPAN-1) (Figure 3C). The cell-cycle arrest, particularly in the G2/M-phases, was not observed in indepKRAS-/BRCA1/2<sup>wild-type</sup> PDAC cell lines (PaTu 8988t and KP-4). Immunoblot analyses showed that COMBO treatment, while effectively reducing PARYlation (Figures 3D and S9A), enhanced the activation of DDR markers such as  $\gamma$ CHK1,  $\gamma$ RPA, and  $\gamma$ H2AX in dKRAS-/BRCA1/2 wild-type PDAC cell lines and dKRAS-/BRCA2 mutant PDAC cells compared to DEC or OLA alone, or to the vehicle DMSO (Figures 3D and S8B–S8D). In contrast, COMBO was ineffective in increasing DDR marker activation in indepKRAS-/BRCA1/2<sup>wild-type</sup> PDAC cell lines compared to OLA or the vehicle alone (Figures 3D and S8B–S8D). Overall, *in vitro* studies demonstrated the antiproliferative efficacy of combining very low-dose DEC with OLA in both dKRAS-/BRCA1/2<sup>wild-type</sup> and dKRAS-/BRCA2<sup>mut</sup> PDAC cells.

### Synergistic antitumor activity of low-dose decitabine with OLA in dKRAS-/BRCA1/2<sup>wild-type</sup> tumor xenograft models

The antitumor activity of the combination treatment was evaluated next. We implanted dKRAS-/BRCA1/2<sup>wild-type</sup> PDAC tumor cells (HPAF-II) or indepKRAS-/BRCA1/2<sup>wild-type</sup> PDAC tumor cells (KP-4 and PaTu 8988t) subcutaneously in NSG-immunodeficient mice. Xenograft tumor models were then subjected to treatment with either vehicle, low-dose DEC (0.2 mg/kg), OLA, or the combination treatment (COMBO). DEC dose (0.2 mg/kg) corresponds to approximately 0.6 mg/m<sup>2</sup> body surface area per day in human, which is 15–30 times lower than the standard clinical dose used to treat human leukemia patients, as per the reference posology. Thus, DEC dose used both as monotherapy and in combination with olaparib, was many-fold reduced compared to standard human posology and thus can be consid-

ered significantly lower than the standard clinical doses. In comparison to higher doses of DEC (1 mg/kg), low-dose DEC (0.2 mg/kg) treatment was well tolerated and exhibited a better safety profile in experimental models (Figure S10A). Results indicated that COMBO treatment led to a significantly synergistic antitumor effect, reducing the growth of dKRAS-/BRCA1/2<sup>wild-type</sup> PDAC xenograft tumors compared to single treatments alone (Figures 4A, 4B and S10B). There were no discernible effects in indepKRAS-/BRCA1/2<sup>wild-type</sup> PDAC xenograft tumors following combined treatment (Figures 4C, 4D, 4E, 4F, S10C, and S10D) when compared to OLA treatment alone. Furthermore, while displaying enhanced antitumor activity, COMBO treatment was well tolerated *in vivo*, as no significant changes in body weight percentage were observed in COMBO-treated mice compared to those receiving single treatment or vehicle alone (Figures S10F–S10I).

Analysis of hematoxylin-eosin-stained lung tissue sections revealed that COMBO treatment exhibited greater antimetastatic effects compared to single drug treatments, as evidenced by a reduction in the number of spontaneous lung metastases generated by dKRAS-/BRCA1/2<sup>wild-type</sup> PDAC xenograft tumors (Figure 4G). Conversely, COMBO treatment showed no significant effects on reducing the number of spontaneous metastases originating from indepKRAS-/BRCA1/2<sup>wild-type</sup> PDAC, with effects limited to OLA alone, but unresponsive to DEC and COMBO (Figures 4H and 4I).

To investigate whether COMBO induced DNA damage *in vivo*, immunohistochemistry (IHC) studies were conducted. Consistent with *in vitro* experiments, COMBO treatment led to increased staining of  $\gamma$ H2AX-positive nuclei in dKRAS-/BRCA1/2<sup>wild-type</sup> PDAC xenograft tumors (Figures 4J and 4K). However, IHC analysis of the same markers in indepKRAS-/BRCA1/2<sup>wild-type</sup> PDAC treated with COMBO showed no significant differences compared to DMSO (vehicle)-treated

### Figure 3. Synergistic combination of low-dose DEC with OLA in dKRAS-PDAC cells

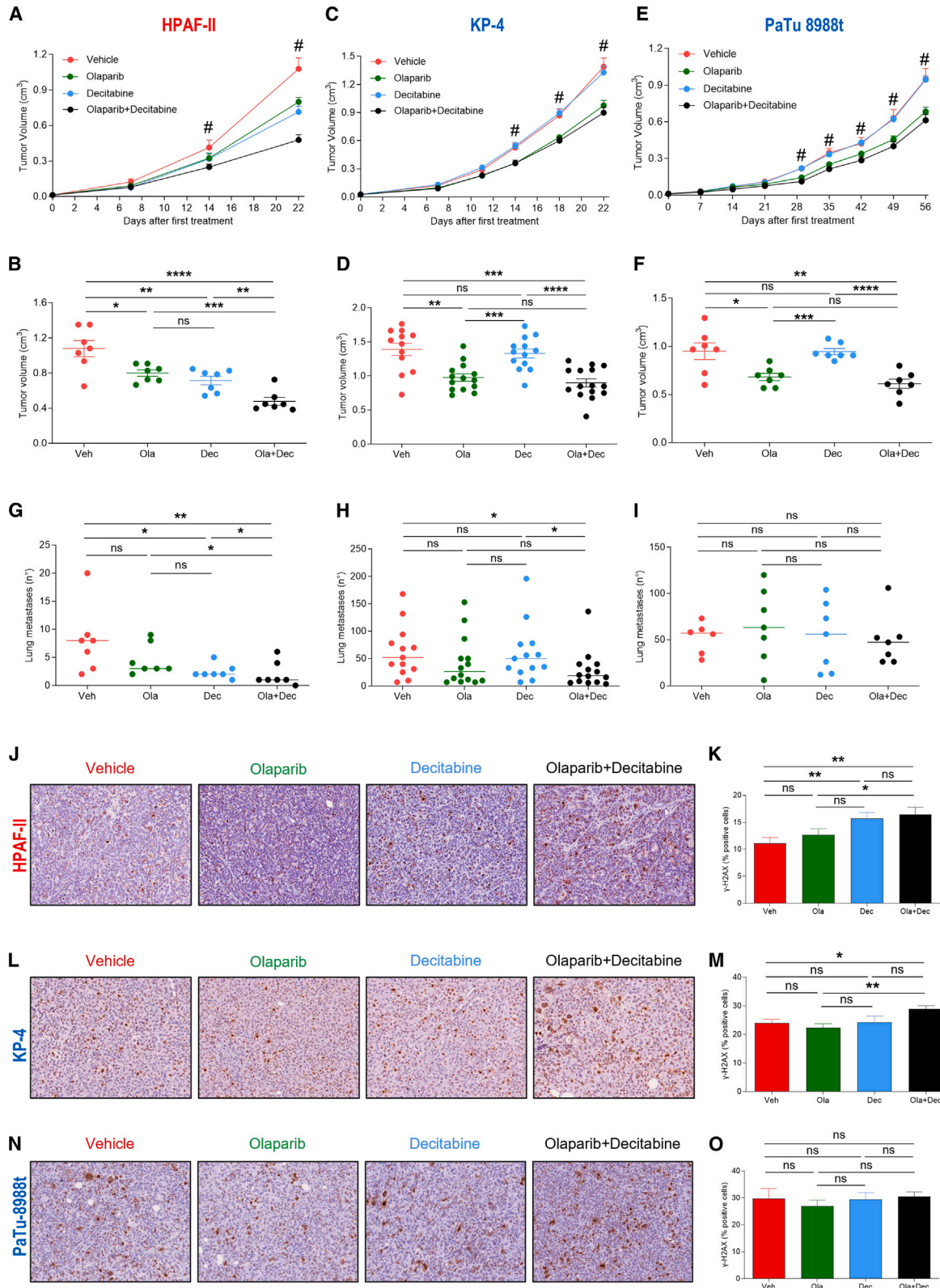
(A) DEC synergizes with OLA. The drug matrix Heatmap, presented in a 4 × 5 grid, illustrates the HAS model index as analyzed by Combeneft methods for pharmacological combination index in dKRAS-/BRCA1/2<sup>wild-type</sup> PDAC cell lines (PaTu 8902, HPAF-II) and dKRAS-/BRCA2<sup>mut</sup> PDAC cells (CAPAN-1). Drug combination doses that exhibit synergy appear blue on the heatmap. The indicated cell lines were plated and grown for 6 days with the specified doses of DEC and OLA. Cell viability was then assessed using the ATP-based CellTiter-Glo assay. Data analysis was conducted using Combeneft software. *n* = 3. Drug concentration ranges were determined based on *in vitro* calculated half-maximal inhibitory concentration (IC<sub>50</sub>) values in each cell line over a seven-day experiment period (Figure S6).

(B) Quantification of comet tail moment (TM) was performed in dKRAS-PDAC cells (PaTu 8902, HPAF-II, and CAPAN-1) and indepKRAS-PDAC cells (PaTu 8988t and KP-4) following 72-h treatment with DMSO, low-dose DEC, OLA, or simultaneous DEC plus OLA (COMBO) at the indicated drug concentrations selected based on Combination Index results (Figure 3A). Data are presented as the median from a representative replicate experiment of the neutral comet assay. At least 200 nuclei were counted for each replicate. To quantify the magnitude of treatment-induced DNA damage among groups, the effect size (e.s.) was estimated using the Wilcoxon test with three biological replicates. The Rstatix package was utilized for the calculation of the effect size. Statistical significance among the indicated comparison groups was determined using the Dunn's test. Statistical significance is denoted by \*\*\*\*, indicating *p* < 0.0001. Medium (M) to large (L) effect sizes suggest substantial DNA damage, while small (S) effect sizes indicate minimal to no response to treatment. The calculated effect sizes indicate a robust induction of DNA damage by COMBO compared to single drugs in dKRAS- cells. No significant increase in TM was observed in indepKRAS cells following COMBO treatment, with effect sizes calculated as small (S). Results of the alkaline comet assay are reported in Figure S8.

(C) Low-dose decitabine in combination with OLA induced a robust cell-cycle block at the G2/M phases of dKRAS-PDAC cells but not of indep-KRAS cells. Cells were treated for 72 h with DMSO, low-dose DEC, OLA, or simultaneous DEC plus OLA (COMBO) at drug concentrations as indicated in (B) and then assayed by FACS analysis of propidium iodide-stained cells. Histograms show mean ± SD (*n* = 3). Statistical significance among treatments was calculated using a one-way ANOVA. # refers to G1-phase; § refers to S-phase; \* refers to G2/M-phase of the cell cycle.

One symbol: *p* ≤ 0.05; two symbols: *p* ≤ 0.01; three symbols: *p* ≤ 0.001; four symbols: *p* ≤ 0.0001.

(D) DDR markers were activated by COMBO treatment, compared to low-dose DEC or OLA alone, in dKRAS-/BRCA1/2<sup>wild-type</sup> PDAC cell lines (PaTu 8902 and HPAF-II) and dKRAS-/BRCA2<sup>mut</sup> PDAC cells (CAPAN-1) but not in indepKRAS-/BRCA1/2<sup>wild-type</sup> PDAC cell lines (PaTu 8988t and KP-4). Immunoblot analysis of  $\gamma$ CHK1(Ser 345),  $\gamma$ RPA32(Ser4/Ser8), and  $\gamma$ H2AX(Ser139) in the indicated cell lines treated for 72 h with DMSO, DEC, OLA, or COMBO at drug concentrations as in (B). Immunoblot for actin was used as a loading control. Numbers below the actin immunoblots represent the ratio of actin densitometry of each sample relative to DMSO. The quantifications of  $\gamma$ CHK1(Ser345),  $\gamma$ RPA32(Ser4/Ser8), and  $\gamma$ H2AX(Ser139) activation are reported in Figure S9.



(legend on next page)

tumors, with effects limited to those elicited by OLA alone (Figures 4L–4O).

### Synergistic antitumor activity of low-dose decitabine with OLA in dKRAS-/BRCA2<sup>mut</sup> PDAC

The results of the *in vitro* combination index assay revealed significant synergy in dKRAS/BRCA2<sup>mut</sup> PDAC cells (CAPAN-1), as COMBO treatment exhibited synergy across all tested drug concentrations. This suggests exceptional efficacy of COMBO in the subgroup of dKRAS-/BRCA2<sup>mut</sup> PDAC, which would already be eligible for OLA treatment. Xenograft tumors derived from CAPAN-1 cells further confirmed that the COMBO treatment displayed higher antitumor activity compared to single treatments (Figures 5A, 5B and S10E). Notably, the combination treatment exhibited significantly greater efficacy against metastasis growth, achieving complete inhibition compared to DEC or OLA alone (Figure 5C). As expected, COMBO treatment led to increased staining of  $\gamma$ H2AX-positive nuclei in xenograft tumors (Figures 5D and 5E). These findings underscore the high synergistic activity of the combination therapy in the context of dKRAS-PDAC tumors already candidates for OLA therapy, where COMBO showed a strong antimetastatic effect.

### KRAS dependency and response to COMBO therapy are not directly associated with HRD biomarkers

To further investigate the predictive value of KRAS dependency for combination treatment with OLA and DEC, we assessed whether the selective efficacy of COMBO treatment could be predicted based on established molecular biomarkers of OLA's antitumor efficacy, such as HRD or BRCAness-like conditions.<sup>19,21</sup> This analysis is crucial to determine if KRAS dependency serves as a unique, independent molecular biomarker for predicting response to COMBO in PDAC. To this aim, we analyzed the genomic mutational profiles of homologous recombination (HR)-related genes in dKRAS- and indepKRAS-PDAC cell lines under investigation in this study using publicly available mutational data from the COSMIC and cBioPortal databases. We searched for both gene mutations and copy-number alterations (CNAs) in genes commonly involved in DDR and homologous recombination, whose mutations are known to be associated with increased OLA cytotoxicity (Figure 6A). Our database inspection revealed that, apart from CAPAN-1 cells harboring germline BRCA2, ATR, and FANCI mutations and PaTu 8988t cells carrying a nonsense mutation in MRE11A, no additional

functionally relevant mutations were found in the selected HR-related genes. Furthermore, no CNAs were detected in HR-related genes in the investigated cell lines, except for BRCA1, FANCI, and MLH1 genes in the CAPAN-1 cell line (Figure 6A). Additionally, we analyzed microsatellite stability (MS) using reported and validated annotations for the overall CCLE panel, and results demonstrated that all investigated cell models exhibited stable microsatellite (MSS) scores (Figure 6A).

We further investigated the status of the so-called "RAD51 score" as a potential cellular biomarker predicting HR functional status, since the RAD51 score has gained interest as a predictor of OLA sensitivity, as detailed in the "Introduction".<sup>23</sup> We estimated the RAD51 score in the panel of PDAC cell lines used for this investigation by immunofluorescence analysis and calculated it as the percentage of RAD51 nuclear foci-positive/Geminin-positive cells. The RAD51 score was demonstrated to be low in the BRCA2-mutated cells, while being high in the HR-proficient cells PANC-1 or in non-transformed human pancreatic epithelial cells (HPDE) carrying the oncogenic KRAS<sup>G72V</sup> mutation (HPDE-KRAS<sup>G72V</sup>), used as a control. The RAD51 score analysis identified a subgroup of cell lines with a high RAD51 score (average score: 41.1%  $\pm$  2.2) and a subgroup of cell lines with a low RAD51 score (average score: 12%  $\pm$  4.6). Results showed no association with KRAS dependency status, as KRAS-dependent models belonged to both the high and low RAD51 groups.

Overall, our findings suggest that KRAS dependency biomarkers, as determined by the L and S scores in PDAC cell lines, are not strictly associated with known HRD biomarkers such as gene mutations in HR-related genes and microsatellite instability. Therefore, KRAS dependency scores may represent an, independent biomarker sufficient to predict response to COMBO treatment in PDAC. However, based on results from the CAPAN-1 and HPAF-II models (Figures 3, 4, and 5), tumor cells carrying both biomarkers, i.e., KRAS dependency with a BRCA2 mutation or low RAD51 score, demonstrated high responsiveness, suggesting that combining dKRAS-dependency scores with HRD biomarkers may be further explored as predictors of drug response, potentially useful for enhancing personalized therapies involving DEC and PARPi.

## DISCUSSION

PDAC remains one of the most lethal solid tumors, with limited treatment options and poor prognosis. The emergence of

### Figure 4. Synergistic antitumor activity of low-dose decitabine with OLA in dKRAS-/BRCA1/2<sup>Wild-Type</sup> tumor xenograft models

(A) Tumor growth kinetics and tumor volume at day 22 (B) of mice injected subcutaneously with the HPAF-II cell line and treated with Vehicle (red line and point), olaparib (green line and point), decitabine (blue line and point), and a combination of olaparib and decitabine (black line and point). Control mice received vehicle treatments both orally and intraperitoneally. Decitabine was administered intraperitoneally at doses of 0.2 mg/kg body weight daily for the first week, followed by three times a week in subsequent weeks. Olaparib was administered orally at a dose of 30 mg/kg body weight daily. Tumor growth (C) and tumor volume at day 22 (D) of mice injected subcutaneously with the KP-4 cell line, following different treatments; tumor growth kinetics (E) and tumor volume at day 56 (F) of mice injected subcutaneously with the PaTu 8988T cell line and treated with the different drugs. The number of lung metastases of mice injected with HPAF-II (G), KP-4 (H), and PaTu 8988t (I) cell lines. Representative images of immunohistochemical staining of  $\gamma$ H2AX marker in sections prepared from HPAF-II tumors (J), KP-4 tumors (L), and PaTu-8988t tumors (N) from each treatment group at the end of the experiments. Histograms show the quantitative evaluation of  $\gamma$ H2AX expressed as a percentage of positive cells in the tumor area of HPAF-II tumors (K), KP-4 tumors (M), and PaTu 8988t tumors (O). Data are represented as mean  $\pm$  SEM (A, B, C, D, E, F, K, M, and O) or median (G, H, and I). Differences in tumor growth kinetics were evaluated using a two-way ANOVA test analysis, while differences in tumor volumes and the percentage of  $\gamma$ H2AX-positive cells were evaluated using unpaired t test analysis; differences in the number of lung metastases were evaluated using Mann-Whitney test analysis.

\*,  $p < 0.05$ ; \*\*,  $p < 0.01$ ; \*\*\*,  $p < 0.001$ ; \*\*\*\*,  $p < 0.0001$ ; ns, not significant.

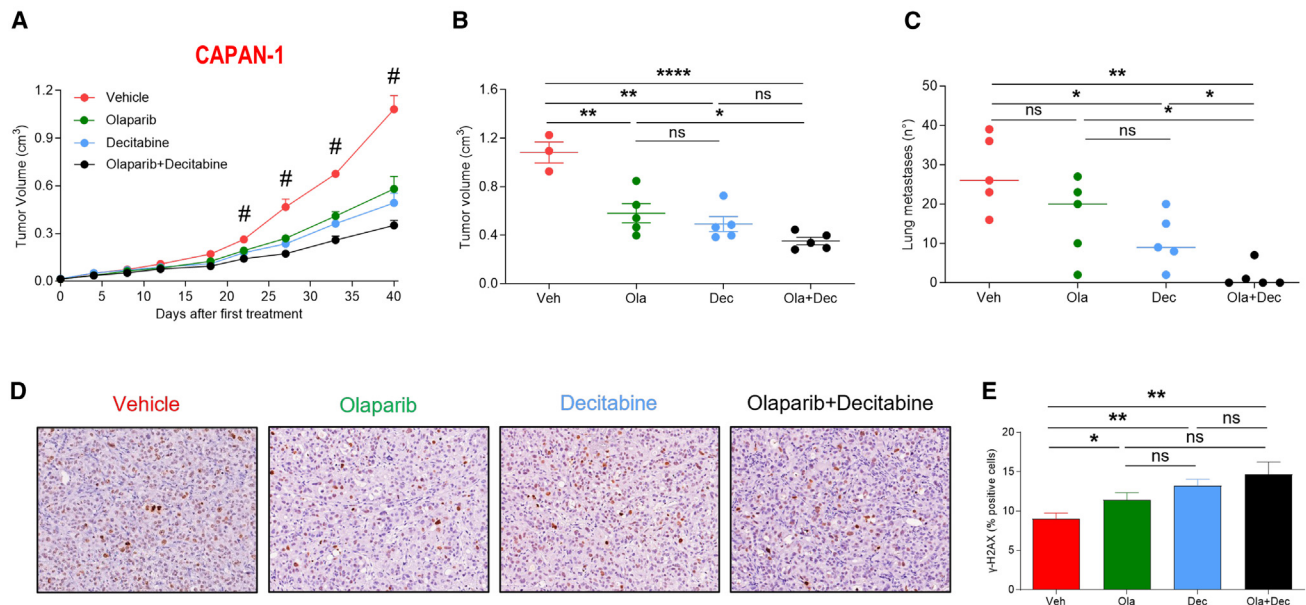


**Figure 5. Synergistic antitumor activity of low-dose decitabine with OLA in dKRAS-/BRCA2<sup>mut</sup> PDAC**

(A) Tumor growth kinetics and tumor volume at day 40 (B), and number of lung metastases (C) in mice injected subcutaneously with the CAPAN-1 cell line and treated with vehicle (red line and point), olaparib (green line and point), decitabine (blue line and point), and a combination of olaparib and decitabine (black line and point). Control mice received vehicle treatments both orally and intraperitoneally. Decitabine was administered intraperitoneally at doses of 0.2 mg/kg body weight daily for the first week, followed by three times a week in subsequent weeks. Olaparib was administered orally at a dose of 30 mg/kg body weight daily. Representative images of immunohistochemical staining of the  $\gamma$ H2AX marker in tumor sections (D), and quantitative evaluation of  $\gamma$ H2AX expression as a percentage of positive cells in the tumor area (E). Data are represented as mean  $\pm$  SEM (A, B, and E) or median (C). Differences in tumor growth kinetics were evaluated using a two-way ANOVA test analysis, while differences in tumor volume and the percentage of  $\gamma$ H2AX-positive cells were evaluated using unpaired test analysis; differences in the number of lung metastases were evaluated using Mann-Whitney test analysis.

\*,  $p < 0.05$ ; \*\*,  $p < 0.01$ ; \*\*\*,  $p < 0.001$ ; \*\*\*\*,  $p < 0.0001$ ; ns, not significant.

personalized medicine has led to a growing interest in identifying targeted therapies for PDAC subtypes, particularly those driven by specific genetic alterations such as KRAS mutations. In this study, we investigated the therapeutic potential of combining DEC with OLA in PDAC, focusing on the subset of tumors exhibiting KRAS dependency. Our findings provide compelling evidence for the synergistic antitumor activity of this combination therapy in KRAS-dependent PDAC models. Notably, the synergistic effect was independent of BRCA mutations, suggesting broader applicability beyond mutated BRCA tumors.

The rationale for combining DEC and OLA stems from their complementary mechanisms of action. DEC induces DNA damage and sensitizes tumor cells to the DNA damage repair inhibitor OLA. Preclinical studies here presented demonstrated that this combination results in enhanced cytotoxicity and antimetastatic effects in KRAS-dependent PDAC models, utilizing low-dose, well-tolerated drug combination regimens of DEC plus OLA. Indeed, the effective dose of DEC tested here, which resulted in a synergistic drug combination with OLA, was 15–30 times lower than the standard doses administered to human leukemia patients on a daily basis. This indicates antitumor effectiveness at a reduced dosage of DEC.

Despite over fifty clinical trials testing the efficacy of decitabine across various cancers, including breast, ovarian, colon, lung, pancreatic cancers, and sarcoma, its toxicity remains a key limiting factor for assessing its antitumor efficacy. FDA-

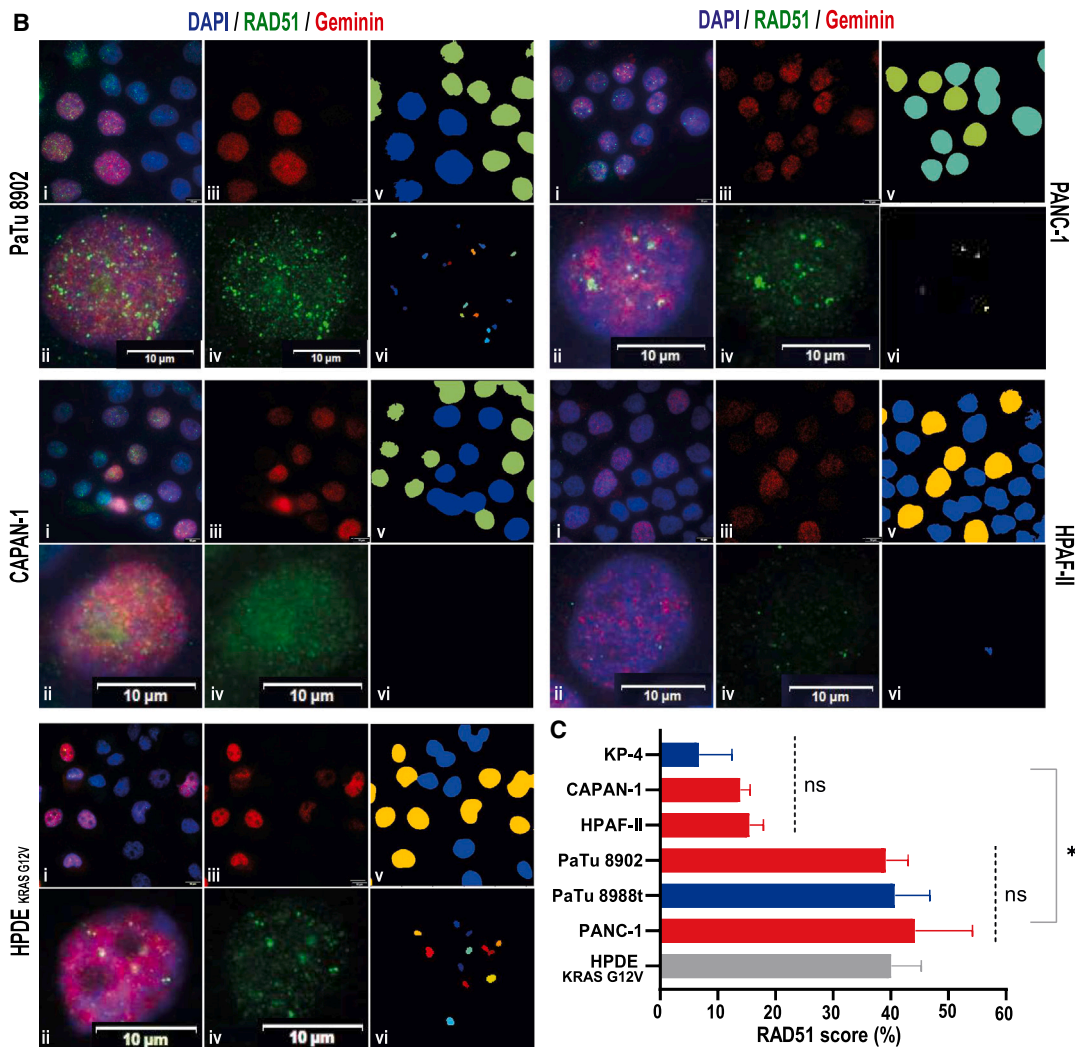
approved regimens are associated with a high rate of hematological toxicity in approximately 30% of cases, including grade 3/4 febrile neutropenia. Importantly, DEC's adverse events may be mitigated by different treatment schemes (such as metronomic dosing) and by reducing dosages<sup>26,27</sup> raising questions about the impact of these changes on its antitumor efficacy. In this context, a combination of synergistic drugs might provide the key. Drug combinations in oncology can improve patient prognosis when a synergistic therapeutic efficacy is achieved. Additionally, synergistic drug combinations at low doses increase the likelihood of achieving drug efficacy at doses that can be readily attained in clinical settings compared to those tested in preclinical studies. Even if the drug synergism observed in preclinical settings results in drug additivity in clinical settings, additivity still represents significant gains in improving therapeutic outcomes.<sup>28</sup> Furthermore, for the COMBO treatment analyzed here, the different hematological toxicity profiles of each drug (i.e., neutropenia for decitabine and anemia for olaparib) are expected to provide more manageable severe adverse events.

From a mechanistic point of view, the combination of OLA and DEC was linked to DEC's ability to induce SSBs and DSBs DNA damage, highlighting its broader potential as an anticancer agent beyond its established role in gene expression regulation. Previously, we reported a molecular mechanism responsible for DEC-induced DNA damage selectively in dKRAS-PDAC.<sup>4</sup> Our studies

A

	PaTu 8902		HPAF-II		CAPAN-1		KP-4		PaTu 8988t		PANC-1	
	CNA	Mutation gene										
KRAS	■	Missense	■	Missense			■	Missense		Missense	■	Missense
PS3		Missense		Missense						Missense		Missense
ATM												
ATR												
BRCA1					■							
BRCA2						Truncating						
CDK12												
CHECK2												
FANCA					■	Truncating						
MLH1												
MRE11A										Truncating		
NBN												
PALB2												
RAD51c												
MSI	inferred-MSS											

B



(legend on next page)

demonstrated that the impairment of *de novo* pyrimidine biosynthesis, leading to DNA damage, due to DEC treatment was a primary mechanism, at least, leading to the selective vulnerability of dKRAS-PDAC cells to decitabine. This conclusion was supported by the following observations: (1) In PDAC, the maintenance of nucleotide pools through pyrimidine biosynthesis is a key feature of the metabolic reprogramming associated with KRAS dependency. This metabolic reprogramming results in a selective reliance of KRAS-dependent PDAC cells on pyrimidine metabolites<sup>29</sup>; (2) The inhibition of pyrimidine biosynthetic enzymes has been shown to reveal a synthetic lethal vulnerability in mutant KRAS-driven cancers<sup>30</sup>; (3) Metabolomic profiling of DEC-treated KRAS-dependent and KRAS-independent PDAC cells demonstrated that DEC impaired *de novo* pyrimidine biosynthesis selectively in dKRAS-PDAC.<sup>4</sup> Specifically, in dKRAS-PDAC cells—but not in KRAS-independent PDAC—decitabine treatment reduced deoxythymidine monophosphate (dTMP) levels while increasing deoxyuridine monophosphate (dUMP) levels and its derivatives. This specific effect on pyrimidine metabolism can increase uracil misincorporation into DNA, thereby causing elevated DNA damage. Additionally, the deamination of decitabine can generate noncanonical aza-dUTP nucleotides,<sup>31</sup> which are incorporated into DNA, recognized as damaged bases, and subsequently trigger extensive uracil glycosylase activity, resulting in DNA breaks.<sup>31,32</sup> Thus, the pyrimidine metabolism dependency of dKRAS-PDAC cells provides at least one plausible explanation for the selective effectiveness of COMBO treatment in KRAS-dependent cell lines. However, we cannot rule out the possibility of additional mechanisms. Further investigation into the molecular basis of KRAS dependency and its interplay with DNA damage response pathways may yield additional insights into other mechanisms linking KRAS dependency with sensitivity to decitabine.

Several other studies have demonstrated that DEC can induce DNA damage in HeLa, colon cancer, and multiple myeloma cells.<sup>14,15</sup> The BER pathway has been implicated, at least in part, in the removal of aberrant bases generated by DEC.<sup>16</sup> The antitumor activity of the decitabine and PARPi combination has substantial mechanistic evidence in tumors other than PDAC. Increased cytotoxic effects of PARP inhibitors with DNA demethylating agents have been reported in unfavorable

AML subtypes and BRCA wild-type breast cancer cells,<sup>24</sup> as well as in breast and ovary cancer<sup>33</sup> and Non-Small Cell Lung Cancer (NSCLC), where DNA methyltransferase inhibitors induced a BRCAness phenotype able to sensitize NSCLC to PARP inhibitor and ionizing radiation<sup>34,35</sup> The cytotoxic activity of covalent PARP1/DNA adducts was also observed in non-transformed human cells following decitabine treatment.<sup>36</sup> Recent studies have further implicated PARP1 activity in DSB repair, where PARP1-DNA co-condensation drives DNA repair site assembly to prevent the disjunction of broken DNA ends.<sup>37</sup> As the formation of chromatin-bound PARP1 is also triggered by PARPi such as talazoparib, it is possible that decitabine might have synergistic activity in dKRAS-PDAC with a broad spectrum of clinically available PARPi.

The rational application of these combination epigenetic approaches in clinic will also require a focus on predictive biomarker discovery to identify molecular and histologic determinants of susceptibility. A phase I clinical trial of the DNA methyltransferase inhibitor decitabine in combination with the PARP inhibitor talazoparib has been conducted in relapsed/refractory acute myeloid leukemia,<sup>38</sup> yet in unselected patients. The efficacy of the COMBO in dKRAS-/BRCA1/2<sup>wild-type</sup> was here predicted using transcriptomic-based KRAS dependency scores as biomarkers of efficacy. We have previously demonstrated that assessing KRAS dependency in PDAC can be achieved using gene expression signature scores in clinical settings (NCT05360264) irrespective of specific KRAS mutations. Given the high prevalence of KRAS-dependent tumors,<sup>4</sup> effective therapies against dKRAS-PDAC, such as COMBO, can offer enhanced therapies for a substantial proportion of PDAC patients.

Furthermore, we found that COMBO was significantly more effective than OLA alone when treating dKRAS-/BRCA2<sup>mut</sup> PDAC cells (CAPAN-1), as demonstrated by two different combination index models showing strong synergistic antiproliferative activity across all analyzed concentrations and by the antimetastatic effect of COMBO in xenograft tumor models. These results suggest that PDAC tumors already candidates for OLA treatment, but classified as KRAS-dependent, might have higher therapeutic benefits from COMBO therapy than OLA treatment alone. There is also the question of whether KRAS dependency

**Figure 6. KRAS dependency and response to COMBO therapy are not directly associated with homologous recombination deficiency (HRD) biomarkers**

(A) Annotation of genomic mutations and gene copy number alterations (CNAs), and inferred Microsatellite (MS) stability status of a panel of HR-related genes in the indicated PDAC cell lines obtained through inspection of the COSMIC and the cBioPortal databases. A red box indicates >2 gene copies. Where indicated, the type of retrieved mutations is annotated. Inferred-MSS: Microsatellite stability, according to previous reports.

(B) Representative immunofluorescence analysis of nuclear RAD51 foci-/Geminin-positive nuclei in a panel of PDAC cell lines for the determination of the “RAD51 score” as a functional biomarker of HR-proficient cells. The nuclei were counterstained with DAPI. Scale bars, 10µm. Magnification, ×60. (i) Representative image of merged nuclear signals for RAD51/DAPI/Geminin; (ii) representative magnification of a single cell as stained in (i); (iii) representative images of Geminin-positive nuclei; (iv) representative magnification of RAD51 nuclear foci; (v) representative image obtained through computational segmentation by CellProfiler 4.2.1 software for Geminin-positive cells and automated cell counting; (vi) representative image obtained through computational segmentation by CellProfiler 4.2.1 software for nuclear RAD51-positive foci for an automated cell counting. PANC-1 is a well-established HR-proficient PDAC cell line; HPDE-KRAS<sup>G12V</sup>: Human Pancreatic Ductal Epithelial cells, stably transfected with oncogenic KRAS<sup>G12V</sup>, here referred to as a control of an HR-proficient cellular model.

(C) Histogram showing RAD51 scores for PDAC cell lines. Blue bars: indepKRAS-cell lines; red bars: dKRAS-cell lines. The “RAD51 score” was calculated as the percentage of RAD51-positive nuclei (≥ 3 nuclear RAD51 foci) over Geminin-positive nuclei. At least 200 nuclei were counted for each replicate by image analysis with CellProfiler 4.2.1 as represented in B. Data are presented as mean ± SD. Statistical analysis was performed using GraphPad Prism. ns: no statistically significant difference within the RAD51 score high group and the RAD51 score low group was calculated by the Kruskal-Wallis test (dotted lines). Statistical significance among the RAD51 score high group versus the RAD51 score low group of cell lines was calculated using a two-way ANOVA test, \*\*\*\*, *p* < 0.0001 (solid line).

might be a molecular phenotype of other solid tumors, such as breast, ovary, and prostate cancer, which have a higher frequency of *BRCA* mutations than PDAC, and if DEC could also enhance the antitumor efficacy of OLA in these tumor subtypes.

We reported that common biomarkers in clinical use or under investigation for predicting response to PARPi do not fully predict the synergistic response to the combination of OLA and DEC compared to KRAS dependency status. Our findings, limited to the cellular models investigated, indicated that KRAS dependency was not associated with common HRD biomarkers or microsatellite instability in PDAC cell lines. Additionally, KRAS dependency scores were not associated with the RAD51 score. Therefore, KRAS dependency appears to be an independent biomarker for predicting response to the OLA and DEC combination treatment in PDAC. Evidence suggests a molecular correlation between HR-repair pathways and KRAS dependency pathways in tumors, particularly in response to radiotherapy,<sup>39</sup> and a correlation between KRAS and RAD51 has been observed in colon cancer.<sup>40</sup> Further investigation into the molecular mechanisms underlying KRAS dependency and its interaction with DNA damage response pathways may provide valuable insights into patient stratification and treatment selection. Furthermore, based on the data presented, it is possible to speculate that combining KRAS dependency scores with biomarkers of HRD, such as genomic alterations of DNA repair genes or RAD51 score, may further refine the selection of patients most likely to respond to therapies with decitabine and PARPi, thus enhancing personalized therapy in PDAC.

While our findings provide preclinical evidence for the efficacy of the DEC+OLA combination in dKRAS-PDAC, several challenges must be addressed to ensure successful translation to clinical practice. First, the partial tumor growth inhibition observed in our *in vivo* models following COMBO treatment suggests that this combination therapy may not achieve complete tumor eradication as a standalone treatment. This highlights the need for further optimization of the therapeutic regimen, potentially through combination with other targeted agents or immune-based therapies which may further enhance the therapeutic impact. Additionally, testing the combination therapy in more physiologically relevant models, such as patient-derived organoids or xenografts, will be essential to better predict clinical outcomes. Second, the repurposing of decitabine in solid tumors such as PDAC presents unique challenges. Although low-dose decitabine was effective in our study, solid tumors generally exhibit complex microenvironments, poor drug penetration, and high intratumoral heterogeneity, all of which may impact treatment efficacy. Third, heterogeneity of KRAS-dependent tumors may influence therapy response and will require further investigation for proper stratification strategies. In conclusion, while the DEC+OLA combination therapy holds promise for extending therapeutic options in dKRAS-PDAC, addressing the challenges of efficacy, toxicity, and patient heterogeneity will be critical for its successful translation to clinical practice.

### Limitations of the study

This study had several limitations that must be addressed, particularly before translating the findings to clinical practice. First, the reliance on tumor xenograft *in vivo* models highlights

the need for validation in more physiologically relevant systems, such as patient-derived organoids or genetically engineered mouse models of spontaneously arising pancreatic cancer, to better predict clinical outcomes. Second, further investigation is required to determine how combination therapy affects the stroma and immune microenvironment of PDAC, as well as how challenges inherent to PDAC—such as complex microenvironments, poor drug penetration, and intratumoral heterogeneity—may limit its efficacy.

### RESOURCE AVAILABILITY

#### Lead contact

Further information and requests for the resources and reagents should be directed to and will be fulfilled by the lead contact, Luca Cardone ([luca.cardone@cnr.it](mailto:luca.cardone@cnr.it)).

#### Materials availability

This study did not generate any new unique reagents and components.

#### Data and code availability

- Genomic data for the pancreatic ductal adenocarcinoma (PDAC) cell lines used in this study are publicly accessible through the Cancer Cell Line Encyclopedia (CCLE) at the CCLE Portal. Additional mutation and copy-number alteration data were obtained from the COSMIC (Catalog Of Somatic Mutations In Cancer) database, accessible at <https://cancer.sanger.ac.uk/cosmic>, and the cBioPortal for Cancer Genomics, accessible at <https://www.cbioportal.org/>. This paper analyzes existing, publicly available gene expression data. Accession numbers are listed in the key resources table.
- This paper does not report original code.
- Any other data supporting the findings of this study are available from the corresponding authors upon request.

### ACKNOWLEDGMENTS

We thank Dr. Giuseppe Diaferia (IFOM, Milan, Italy) for providing some PDAC cell lines. We also thank Dr. A. Cavazzani (University of Tor Vergata, Rome) and Dr. C. Angelini (IAC-CNR) for their support in statistical analysis. We are grateful to Dr. V. Marabitti for technical advice on comet assay protocols, and Dr. A. Torcinaro (IBBC-CNR) for advice on CellProfiler software. We thank Dr. C. di Pietro (IBBC-CNR) for technical support with confocal microscopy, and Dr. G. Pfister (EMBL-Monterotondo, Rome) and Dr. A. Giovinazzo (IBBC-CNR) for advice and support with flow cytometry analysis.

G.A. and M.F. were supported by fellowships from Associazione “Nastro Viola”, Italy. This work was supported by LILT, Italy, Intramural grants of Regina Elena National Cancer Institute (IRE), Italy, and Associazione “Nastro Viola”, Italy.

The study was supported by a grant to Dr. Alessia Lamolinara financed by “Unione europea – NextGenerationEU”, “Programma MUR-Fondo Promozione e Sviluppo - DM 737/202”, Acronym “PDAC-TREAT”, title “Testing repurposed drugs candidates in pancreatic ductal adenocarcinomas: a multi-level *in vitro/in vivo* approach for improved therapy.”

### AUTHOR CONTRIBUTIONS

G.A., M.F., and A.L. conducted experiments, developed methodologies, and analyzed data, including statistical analysis, as well as interpreted results. M.F. specifically performed imaging analysis, while C.M. and F.d.M. assisted in certain experiments. M.M. and M.F. performed the computational analysis of KRAS-dependency scores. M.I. oversaw *in vivo* studies, contributed to discussions, data analysis, and methodology development. L.C., G.A., and M.F. designed and conceived the study. L.C. supervised the study, edited the manuscript draft, and provided overall guidance and financial support for

the project. All authors thoroughly reviewed and contributed to the final version of the manuscript.

#### DECLARATION OF INTERESTS

The authors declare no competing interests.

#### DECLARATION OF GENERATIVE I AND AI-ASSISTED TECHNOLOGIES IN THE WRITING PROCESS

During the preparation of this work, the authors used ChatGPT (GPT-4) of OpenAI for proofreading and to improve readability. After using this service, the authors reviewed and edited the content as needed and take full responsibility for the content of the publication.

#### STAR★METHODS

Detailed methods are provided in the online version of this paper and include the following:

- KEY RESOURCES TABLE
- EXPERIMENTAL MODEL AND STUDY PARTICIPANT DETAILS
  - Cell lines
  - Animal studies
- METHOD DETAILS
  - Reagents and chemicals
  - KRAS dependency signature score calculation methods
  - Cell viability assay and half-maximal inhibitory concentration (IC50) determination
  - Comet assay
  - Solutions
  - Cell cycle analysis by flow cytometry
  - Immunofluorescence analysis of DDR markers
  - RAD51 score
  - Genomic data analysis and microsatellite stability assessment
  - Subcellular protein fractions
  - Total cell lysates
  - "Combeneft" method for drug combination index analysis
  - "Calculusyn" method for drug combination index analysis
  - Immunoblot analysis
  - Methods for human equivalent dose (HED) calculation
  - Histological and immunohistochemical analysis
- QUANTIFICATION AND STATISTICAL ANALYSIS

#### SUPPLEMENTAL INFORMATION

Supplemental information can be found online at <https://doi.org/10.1016/j.isci.2025.111842>.

Received: June 27, 2024

Revised: December 9, 2024

Accepted: December 16, 2024

Published: January 20, 2025

#### REFERENCES

1. Siegel, R.L., Giaquinto, A.N., Jemal, A. (2024). Cancer statistics. *CA Cancer J. Clin.* *74*, 12–49. <https://doi.org/10.3322/caac.21820>. Erratum in 2024. *CA Cancer J. Clin.* *74*, 203. <https://doi.org/10.3322/caac.21830>.
2. Kanda, M., Matthaei, H., Wu, J., Hong, S.-M., Yu, J., Borges, M., Hruban, R.H., Maitra, A., Kinzler, K., Vogelstein, B., and Goggins, M. (2012). Presence of somatic mutations in most early-stage pancreatic intraepithelial neoplasia. *Gastroenterology* *142*, 730–733.e9. <https://doi.org/10.1053/j.gastro.2011.12.042>.
3. Collins, M.A., Bednar, F., Zhang, Y., Brisset, J.-C., Galbán, S., Galbán, C.J., Rakshit, S., Flannagan, K.S., Adsay, N.V., and Pasca di Magliano, M. (2012). Oncogenic Kras is required for both the initiation and maintenance of pancreatic cancer in mice. *J. Clin. Invest.* *122*, 639–653. <https://doi.org/10.1172/JCI59227>.
4. Mottini, C., Tomihara, H., Carrella, D., Lamolinara, A., Iezzi, M., Huang, J.K., Amoreo, C.A., Buglioni, S., Manni, I., Robinson, F.S., et al. (2019). Predictive Signatures Inform the Effective Repurposing of Decitabine to Treat KRAS-Dependent Pancreatic Ductal Adenocarcinoma. *Cancer Res.* *79*, 5612–5625. <https://doi.org/10.1158/0008-5472.CAN-19-0187>.
5. Singh, A., Greninger, P., Rhodes, D., Koopman, L., Violette, S., Bardeesy, N., and Settleman, J. (2009). A gene expression signature associated with "K-Ras addiction" reveals regulators of EMT and tumor cell survival. *Cancer Cell* *15*, 489–500. <https://doi.org/10.1016/j.ccr.2009.03.022>.
6. Gupta, S.C., Sung, B., Prasad, S., Webb, L.J., and Aggarwal, B.B. (2013). Cancer drug discovery by repurposing: teaching new tricks to old dogs. *Trends Pharmacol. Sci.* *34*, 508–517. <https://doi.org/10.1016/j.tips.2013.06.005>.
7. Mottini, C., Napolitano, F., Li, Z., Gao, X., and Cardone, L. (2021). Computer-aided drug repurposing for cancer therapy: Approaches and opportunities to challenge anticancer targets. *Semin. Cancer Biol.* *68*, 59–74. <https://doi.org/10.1016/j.semcancer.2019.09.023>.
8. Ye, C., Jiang, N., Zheng, J., Zhang, S., Zhang, J., and Zhou, J. (2024). Epigenetic therapy: Research progress of decitabine in the treatment of solid tumors. *Biochim. Biophys. Acta Rev. Canc* *1879*, 189066. <https://doi.org/10.1016/j.bbcan.2023.189066>.
9. Stewart, D.J., Issa, J.-P., Kurzrock, R., Nunez, M.I., Jelinek, J., Hong, D., Oki, Y., Guo, Z., Gupta, S., and Wistuba, I.I. (2009). Decitabine Effect on Tumor Global DNA Methylation and Other Parameters in a Phase I Trial in Refractory Solid Tumors and Lymphomas. *Clin. Cancer Res.* *15*, 3881–3888. <https://doi.org/10.1158/1078-0432.CCR-08-2196>.
10. Christman, J.K. (2002). 5-Azacytidine and 5-aza-2'-deoxycytidine as inhibitors of DNA methylation: mechanistic studies and their implications for cancer therapy. *Oncogene* *21*, 5483–5495. <https://doi.org/10.1038/sj.onc.1205699>.
11. Matei, D., Fang, F., Shen, C., Schilder, J., Arnold, A., Zeng, Y., Berry, W.A., Huang, T., and Nephew, K.P. (2012). Epigenetic Resensitization to Platinum in Ovarian Cancer. *Cancer Res.* *72*, 2197–2205. <https://doi.org/10.1158/0008-5472.CAN-11-3909>.
12. Goyal, A., Bauer, J., Hey, J., Papageorgiou, D.N., Stepanova, E., Daskalakis, M., Scheid, J., Dubbelaar, M., Klimovich, B., Schwarz, D., et al. (2023). DNMT and HDAC inhibition induces immunogenic neoantigens from human endogenous retroviral element-derived transcripts. *Nat. Commun.* *14*, 6731. <https://doi.org/10.1038/s41467-023-42417-w>.
13. Ghoneim, H.E., Fan, Y., Moustaki, A., Abdelsamed, H.A., Dash, P., Dogra, P., Carter, R., Awad, W., Neale, G., Thomas, P.G., and Youngblood, B. (2017). De Novo Epigenetic Programs Inhibit PD-1 Blockade-Mediated T Cell Rejuvenation. *Cell* *170*, 142–157.e19. <https://doi.org/10.1016/j.cell.2017.06.007>.
14. Pali, S.S., Van Emburgh, B.O., Sankpal, U.T., Brown, K.D., and Robertson, K.D. (2008). DNA Methylation Inhibitor 5-Aza-2'-Deoxycytidine Induces Reversible Genome-Wide DNA Damage That Is Distinctly Influenced by DNA Methyltransferases 1 and 3B. *Mol. Cell Biol.* *28*, 752–771. <https://doi.org/10.1128/MCB.01799-07>.
15. Maes, K., De Smedt, E., Lemaire, M., De Raeye, H., Menu, E., Van Valckenborgh, E., McClue, S., Vanderkerken, K., and De Bruyne, E. (2014). The role of DNA damage and repair in decitabine-mediated apoptosis in multiple myeloma. *Oncotarget* *5*, 3115–3129. <https://doi.org/10.18632/oncotarget.1821>.
16. Orta, M.L., Höglund, A., Calderón-Montaño, J.M., Domínguez, I., Burgos-Morón, E., Visnes, T., Pastor, N., Ström, C., López-lázaro, M., and Helleday, T. (2014). The PARP inhibitor Olaparib disrupts base excision repair of 5-aza-2'-deoxycytidine lesions. *Nucleic Acids Res.* *42*, 9108–9120. <https://doi.org/10.1093/nar/gku638>.
17. Yabushita, T., Chinen, T., Nishiyama, A., Asada, S., Shimura, R., Isobe, T., Yamamoto, K., Sato, N., Enomoto, Y., Tanaka, Y., et al. (2023). Mitotic

- perturbation is a key mechanism of action of decitabine in myeloid tumor treatment. *Cell Rep.* 42, 113098. <https://doi.org/10.1016/j.celrep.2023.113098>.
18. Ray Chaudhuri, A., and Nussenzweig, A. (2017). The multifaceted roles of PARP1 in DNA repair and chromatin remodelling. *Nat. Rev. Mol. Cell Biol.* 18, 610–621. <https://doi.org/10.1038/nrm.2017.53>.
  19. Rose, M., Burgess, J.T., O'Byrne, K., Richard, D.J., and Bolderson, E. (2020). PARP Inhibitors: Clinical Relevance, Mechanisms of Action and Tumor Resistance. *Front. Cell Dev. Biol.* 8, 564601. <https://doi.org/10.3389/fcell.2020.564601>.
  20. Antolin, A.A., Ameratunga, M., Banerji, U., Clarke, P.A., Workman, P., and Al-Lazikani, B. (2020). The kinase polypharmacology landscape of clinical PARP inhibitors. *Sci. Rep.* 10, 2585. <https://doi.org/10.1038/s41598-020-59074-4>.
  21. Casolino, R., Paiella, S., Azzolina, D., Beer, P.A., Corbo, V., Lorenzoni, G., Gregori, D., Golan, T., Braconi, C., Froeling, F.E.M., et al. (2021). Homologous Recombination Deficiency in Pancreatic Cancer: A Systematic Review and Prevalence Meta-Analysis. *J. Clin. Oncol.* 39, 2617–2631. <https://doi.org/10.1200/JCO.20.03238>.
  22. Golan, T., Stossel, C., Atias, D., Buzhor, E., Halperin, S., Cohen, K., Raites-Gurevich, M., Glick, Y., Raskin, S., Yehuda, D., et al. (2018). Recapitulating the clinical scenario of BRCA-associated pancreatic cancer in pre-clinical models. *Int. J. Cancer* 143, 179–183. <https://doi.org/10.1002/ijc.31292>.
  23. Castroviejo-Bermejo, M., Cruz, C., Llop-Guevara, A., Gutiérrez-Enríquez, S., Ducy, M., Ibrahim, Y.H., Gris-Oliver, A., Pellegrino, B., Bruna, A., Guzmán, M., et al. (2018). A RAD51 assay feasible in routine tumor samples calls PARP inhibitor response beyond BRCA mutation. *EMBO Mol. Med.* 10, e9172. <https://doi.org/10.15252/emmm.201809172>.
  24. Muvarak, N.E., Chowdhury, K., Xia, L., Robert, C., Choi, E.Y., Cai, Y., Bellani, M., Zou, Y., Singh, Z.N., Duong, V.H., et al. (2016). Enhancing the Cytotoxic Effects of PARP Inhibitors with DNA Demethylating Agents – A Potential Therapy for Cancer. *Cancer Cell* 30, 637–650. <https://doi.org/10.1016/j.ccell.2016.09.002>.
  25. Wei, L., Nakajima, S., Hsieh, C.-L., Kanno, S., Masutani, M., Levine, A.S., Yasui, A., and Lan, L. (2013). Damage response of XRCC1 at sites of DNA single strand breaks is regulated by phosphorylation and ubiquitylation after degradation of poly(ADP-ribose). *J. Cell Sci.* 126, 4414–4423. <https://doi.org/10.1242/jcs.128272>.
  26. Jan, N., Sofi, S., Qayoom, H., Shabir, A., Haq, B.U., Macha, M.A., Almilabary, A., and Mir, M.A. (2024). Metronomic chemotherapy and drug repurposing: A paradigm shift in oncology. *Heliyon* 10, e24670. <https://doi.org/10.1016/j.heliyon.2024.e24670>.
  27. Kishtagari, A., Awada, H., Mahfouz, R.Z., Kuzmanovic, T., Durrani, J., Kerr, C.M., Patel, B.J., Visconte, V., Radivoyevitch, T., Lichtin MD, A., et al. (2019). Extended Experience with a Very Low Dose, Metronomic, Subcutaneous Decitabine Regimen Intended to Deplete DNMT1 without Cytotoxicity. *Blood* 134, 1279. <https://doi.org/10.1182/blood-2019-130579>.
  28. Hwangbo, H., Patterson, S.C., Dai, A., Plana, D., and Palmer, A.C. (2023). Additivity predicts the efficacy of most approved combination therapies for advanced cancer. *Nat. Can. (Ott.)* 4, 1693–1704. <https://doi.org/10.1038/s43018-023-00667-z>.
  29. Santana-Codina, N., Roeth, A.A., Zhang, Y., Yang, A., Mashadova, O., Asara, J.M., Wang, X., Bronson, R.T., Lyssiotis, C.A., Ying, H., and Kimmelman, A.C. (2018). Oncogenic KRAS supports pancreatic cancer through regulation of nucleotide synthesis. *Nat. Commun.* 9, 4945. <https://doi.org/10.1038/s41467-018-07472-8>.
  30. Koundinya, M., Sudhalter, J., Courjaud, A., Lionne, B., Touyer, G., Bonnet, L., Menguy, I., Schreiber, I., Perrault, C., Vouquier, S., et al. (2018). Dependence on the Pyrimidine Biosynthetic Enzyme DHODH Is a Synthetic Lethal Vulnerability in Mutant KRAS-Driven Cancers. *Cell Chem. Biol.* 25, 705–717.e11. <https://doi.org/10.1016/j.chembiol.2018.03.005>.
  31. Requena, C.E., Pérez-Moreno, G., Horváth, A., Vértessy, B.G., Ruiz-Pérez, L.M., González-Pacanoska, D., and Vidal, A.E. (2016). The nucleotidohydrolases DCTPP1 and dUTPase are involved in the cellular response to decitabine. *Biochem. J.* 473, 2635–2643. <https://doi.org/10.1042/BCJ20160302>.
  32. Boorstein, R.J., Chiu, L.-N., and Teebor, G.W. (1992). A Mammalian Cell Line Deficient in Activity of the DNA Repair Enzyme 5-Hydroxymethyluracil-DNA Glycosylase Is Resistant to the Toxic Effects of the Thymidine Analog 5-Hydroxymethyl-2'-Deoxyuridine. *Mol. Cell Biol.* 12, 5536–5540. <https://doi.org/10.1128/mcb.12.12.5536-5540.1992>.
  33. Pulliam, N., Fang, F., Ozes, A.R., Tang, J., Adewuyi, A., Keer, H., Lyons, J., Baylin, S.B., Matei, D., Nakshatri, H., et al. (2018). An Effective Epigenetic-PARP Inhibitor Combination Therapy for Breast and Ovarian Cancers Independent of BRCA Mutations. *Clin. Cancer Res.* 24, 3163–3175. <https://doi.org/10.1158/1078-0432.CCR-18-0204>.
  34. Abbotts, R., Topper, M.J., Biondi, C., Fontaine, D., Goswami, R., Stojanovic, L., Choi, E.Y., McLaughlin, L., Kogan, A.A., Xia, L., et al. (2019). DNA methyltransferase inhibitors induce a BRCAness phenotype that sensitizes NSCLC to PARP inhibitor and ionizing radiation. *USA* 116, 22609–22618. <https://doi.org/10.1073/pnas.1903765116>.
  35. Lok, B.H., and Rudin, C.M. (2019). Epigenetic targeting of DNA repair in lung cancer. *USA* 116, 22429–22431. <https://doi.org/10.1073/pnas.1916581116>.
  36. Kiianitsa, K., Zhang, Y., and Maizels, N. (2020). Treatment of human cells with 5-aza-dC induces formation of PARP1-DNA covalent adducts at genomic regions targeted by DNMT1. *DNA Repair* 96, 102977. <https://doi.org/10.1016/j.dnarep.2020.102977>.
  37. Chappidi, N., Quail, T., Doll, S., Vogel, L.T., Aleksandrov, R., Felekyan, S., Kühnemuth, R., Stoyanov, S., Seidel, C.A.M., Brugués, J., et al. (2024). PARP1-DNA co-condensation drives DNA repair site assembly to prevent disjunction of broken DNA ends. *Cell* 187, 945–961.e18. <https://doi.org/10.1016/j.cell.2024.01.015>.
  38. Baer, M.R., Kogan, A.A., Bentzen, S.M., Mi, T., Lapidus, R.G., Duong, V.H., Emadi, A., Niyongere, S., O'Connell, C.L., Youngblood, B.A., et al. (2022). Phase I Clinical Trial of DNA Methyltransferase Inhibitor Decitabine and PARP Inhibitor Talazoparib Combination Therapy in Relapsed/Refractory Acute Myeloid Leukemia. *Clin. Cancer Res.* 28, 1313–1322. <https://doi.org/10.1158/1078-0432.CCR-21-3729>.
  39. Toulany, M. (2023). Targeting K-Ras-mediated DNA damage response in radiation oncology: Current status, challenges and future perspectives. *Clin. Transl. Radiat. Oncol.* 38, 6–14. <https://doi.org/10.1016/j.ctro.2022.10.004>.
  40. Kalimutho, M., Bain, A.L., Mukherjee, B., Nag, P., Nanayakkara, D.M., Harten, S.K., Harris, J.L., Subramanian, G.N., Sinha, D., Shirasawa, S., et al. (2017). Enhanced dependency of KRAS -mutant colorectal cancer cells on RAD 51-dependent homologous recombination repair identified from genetic interactions in *Saccharomyces cerevisiae*. *Mol. Oncol.* 11, 470–490. <https://doi.org/10.1002/1878-0261.12040>.
  41. Barretina, J., Caponigro, G., Stransky, N., Venkatesan, K., Margolin, A.A., Kim, S., Wilson, C.J., Lehár, J., Kryukov, G.V., Sonkin, D., et al. (2012). The Cancer Cell Line Encyclopedia enables predictive modelling of anticancer drug sensitivity. *Nature* 483, 603–607. <https://doi.org/10.1038/nature11003>.
  42. Ghandi, M., Huang, F.W., Jané-Valbuena, J., Kryukov, G.V., Lo, C.C., McDonald, E.R., Barretina, J., Gelfand, E.T., Bielski, C.M., Li, H., et al. (2019). Next-generation characterization of the Cancer Cell Line Encyclopedia. *Nature* 569, 503–508. <https://doi.org/10.1038/s41586-019-1186-3>.
  43. Reagan-Shaw, S., Nihal, M., and Ahmad, N. (2008). Dose translation from animal to human studies revisited. *Faseb. J.* 22, 659–661. <https://doi.org/10.1096/fj.07-9574LSF>.

## STAR★METHODS

### KEY RESOURCES TABLE

REAGENT or RESOURCE	SOURCE	IDENTIFIER
<b>Antibodies</b>		
Phospho-Histone H2AX (Ser139)	Merck Millipore	Cat#05-636; RRID: AB_309864
Rabbit polyclonal XRCC1 Antibody	Cell Signaling Technology	Cat#2735; RRID: AB_2218471
Anti-Rad51	Abcam	Ab133534; RRID: AB_2722613
53BP1	Novus Biologicals	NB100-305; RRID: AB_10001695
phospho-Chk1 (Ser345) (133D3)	Cell Signaling Technology	Cat#2348; RRID: AB_331212
PARP1 (46D11) Rabbit mAb	Cell Signaling Technology	Cat#9532; RRID: AB_659884
PAR/pADPr Antibody	R&D Systems	Cat#4335-MC-100; RRID: AB_3644339
β-Actin Antibody	Sigma-Aldrich	No. SAB5600204; RRID: AB_3097735
Histone H3 (D1H2) XPR Rabbit mAb	Cell Signaling Technology	Cat#4499; RRID: AB_10544537
CHK1 (2G1D5) Mouse mAb	Cell Signaling Technology	Cat#2360; RRID: AB_2080320
Phospho-RPA32 (S4/S8)	Bethyl Laboratories	A300-245A; RRID: AB_210547
Phospho-Chk1 (S317)	Cell Signaling Technology	Cat#2344; RRID: AB_331488
Phospho-Chk2 (Thr68)	Cell Signaling Technology	Cat#2661; RRID: AB_331479
Chk2 (1C12) Mouse mAb	Cell Signaling Technology	Cat#3440; RRID: AB_2229490
RCC1 (N-19)	Santa Cruz Biotechnology	sc-1161; RRID: AB_632319
Alexa Fluor 488 donkey anti-rabbit antibody	Thermo Fisher Scientific	R37118; RRID: AB_2556546
Alexa Fluor 594 donkey anti-mouse antibody	Thermo Fisher Scientific	R37115; RRID: AB_2556543
Goat Anti-rabbit IgG, HRP-linked antibody	Cell Signaling Technology	Cat#7074; RRID: AB_2099233
Anti-mouse IgG	Bethyl Laboratories	A90-116P; RRID: AB_67183
K-Ras (F234)	Santa Cruz Biotechnology	SC-30; RRID: AB_627865
p-ERK 1/2 (Thr 202/Tyr 204)	Santa Cruz Biotechnology	SC-16982-R; RRID: AB_653182
Pan-Ras	Cell Signaling Technology	Cat#8832
Geminin-L-CE primary antibody	Leica Biosystems	Geminin-L-CE
<b>Chemicals, peptides, and recombinant proteins</b>		
Decitabine (5-Aza-2'-deoxycytidine)	Sigma-Aldrich	A3656
Dimethyl Sulfoxide (DMSO)	Sigma-Aldrich	D2438
Protease Inhibitor Cocktail	Sigma-Aldrich	P8340
Bovine Serum Albumin	Sigma-Aldrich	A4503
β-Nicotinamide adenine dinucleotide (NAD <sup>+</sup> )	Sigma-Aldrich	N8410
Olaparib (AZD2281, KU-0059436)	Selleckchem	S1060
AZD1390 (ATM inhibitor)	Selleckchem	S8680
Elimusertib (BAY-1895344)	Selleckchem	S9864
Poly(ADP-ribose) Glycohydrolase (PARG) inhibitor: PDD00017273	MedChemExpress	HY-108360
Matrigel	BD Biosciences	Cat#211242
DMEM (1X) + GlutaMAX™-I	Gibco	Cat#31966-021
Iscove's modified Dulbecco's medium (IMDM)	Gibco	Cat#21980-032
RPMI 1640	Euroclone	ECB9006L
Fetal Bovine Serum (FBS)	Gibco	A5256701
Penicillin–Streptomycin (Pen Strep)	Gibco	Cat#15140-122
L-Glutamine 100X	EuroClone	Cat#ECB3000D

(Continued on next page)

**Continued**

REAGENT or RESOURCE	SOURCE	IDENTIFIER
PBS	EuroClone	Cat#ECB4004L
Fixative Solution (4% formaldehyde)	Invitrogen	FB002
Triton X-100	Sigma-Aldrich	T9284
Fluoroshield™ with DAPI	Sigma-Aldrich	F6057
Micrococcal Nuclease	Thermo Fisher Scientific	Cat#88216
Protein Assay Dye Reagent Concentrate	Bio-Rad	Cat#5000006
RIPA Buffer (10X)	Cell Signaling Technology	Cat#9806

**Critical commercial assays**

CellTiter-Glo Luminescent Cell Viability Assay	Promega	Cat#G7570
FxCycle™ PI/RNase Staining Solution	Thermo Fisher Scientific	Cat#F10797
MycoFluor Mycoplasma Detection Kit	Thermo Fisher Scientific	Cat#M7006
Novex™ 4-20%, Tris-Glycine Plus WedgeWell™ Gel	Invitrogen	XP04202BOX
Novex™ 4-12%, Tris-Glycine Mini WedgeWell™ Gel	Invitrogen	XP04120BOX
Nitrocellulose Membranes Amersham™ Protran™ 0.45µm NC	Sigma-Aldrich	GE10600002

**Experimental models: Cell lines**

Human: CAPAN-1	Dr. Giuseppe Diaferia (IEO, Milan, Italy)	RRID:CVCL_0237
Human: CAPAN-2	ATCC	Cat#HTB-80, RRID:CVCL_0026
Human: BxPC3	Dr. Giuseppe Diaferia (IEO, Milan, Italy)	RRID:CVCL_0186
Human: AspC1	Dr. Giuseppe Diaferia (IEO, Milan, Italy)	RRID:CVCL_0152
Human: PaTu 8902	Dr. Giuseppe Diaferia (IEO, Milan, Italy)	RRID:CVCL_1845
Human: KP-4	UTMDACC; Houston, Texas	RRID:CVCL_1338
Human: PaTu 8988t	UTMDACC; Houston, Texas	RRID:CVCL_1847
Human: HPAF-II	Dr. Michele Milella (University of Verona; Italy)	RRID:CVCL_0313
Human: SU8686	ATCC	Cat#CRL-1837, RRID:CVCL_3881
Human: HPDE	Dr. Melisi (University of Verona, Italy)	RRID:CVCL_4376

**Experimental models: Organisms/strains**

Mouse: NOD.Cg-Prkdcscid Il2rgtm1Wjl/SzJ (NSG)	The Jackson Laboratory and bred in the animal facility of CAST (G. D'Annunzio University, Chieti, Italy)	RRID:IMSR_JAX:005557
---	--	----------------------

**Deposited data**

Gene expression data	Barretina et al. <sup>41</sup>	GEO GSE36133
Genomic data and MSI status	Ghandi et al. <sup>42</sup>	–
Genomic and CNA data	COSMIC	<a href="https://cancer.sanger.ac.uk/cell_lines">https://cancer.sanger.ac.uk/cell_lines</a>
Genomic and CNA data	cBioPortal	<a href="https://www.cbioportal.org/">https://www.cbioportal.org/</a>

**Software and algorithms**

Combeneft	<a href="https://www.cruk.cam.ac.uk/research-groups/jodrell-group/combeneft">https://www.cruk.cam.ac.uk/research-groups/jodrell-group/combeneft</a>	–
FlowJo v10.7.2	BD Bioscience	<a href="https://www.flowjo.com/solutions/flowjo">https://www.flowjo.com/solutions/flowjo</a>
ImageJ	NIH	<a href="https://imagej.nih.gov/ij//index.html">https://imagej.nih.gov/ij//index.html</a>
CalcuSyn	dkNET	<a href="http://www.biosoft.com/w/calculusyn.htm">http://www.biosoft.com/w/calculusyn.htm</a> RRID: SCR_020251
GraphPad Prism 8.0	GraphPad	<a href="https://www.graphpad.com/">https://www.graphpad.com/</a>
CellProfiler	CellProfiler	<a href="http://www.cellprofiler.org">www.cellprofiler.org</a>

(Continued on next page)

**Continued**

REAGENT or RESOURCE	SOURCE	IDENTIFIER
Comet Score™ software	TriTek Corp	<a href="http://rexhoover.com/cometscore.php">http://rexhoover.com/cometscore.php</a>
RStudio	R core team	<a href="http://www.rstudio.com/">http://www.rstudio.com/</a>
QuPath 0.3.2 software	GitHub	<a href="https://qupath.github.io">https://qupath.github.io</a>

**EXPERIMENTAL MODEL AND STUDY PARTICIPANT DETAILS**

**Cell lines**

All the cells used in this study are of human origin. CAPAN-1, BXPc3, ASPC1, and PaTu 8902 cell lines were provided by Dr. Giuseppe Diaferia (European Institute of Oncology, Milan, Italy). KP-4 and PaTu 8988t cell lines were provided by the cell culture facility at The University of Texas MD Anderson Cancer Center (UTMDACC; Houston, Texas). HPAF-II cell lines were provided by Dr. Michele Milella (Department of Medicine, University of Verona, Italy). The SU8686 cell line was purchased from ATCC. Human pancreatic ductal epithelia (HPDE) KRAS<sup>G12V</sup> isogenic derivatives were obtained from Dr. D. Melisi (Department of Medicine, University of Verona, Italy). Cell line identities were genetically validated according to relative cell bank procedures and were cultured for fewer than 6 weeks after resuscitation. Additionally, full transcriptomic profiles from the cell lines under investigation were routinely analyzed and compared with reference transcriptomic profiles derived from multiple references in publicly available databases (GEO), to assess the global genetic identity. Upon passage 10, cells were discarded. All cells were routinely tested for Mycoplasma contamination using a MycoFluor Mycoplasma Detection Kit (Thermo Fisher Scientific).

PaTu 8902 and PaTu 8988t cells were maintained in DMEM high glucose containing L-glutamine and sodium pyruvate, supplemented with 10% FBS (Gibco). CAPAN-1 cells were grown in RPMI supplemented with 20% FBS (Gibco) plus 1% glutamine (Gibco). KP-4 cells were maintained in Iscove's modified Dulbecco's medium (Gibco), supplemented with 20% FBS and 200 mmol/L glutamine. SU8686, HPAF-II, BxPC-3, HPDE and ASPC1 cells were maintained in RPMI supplemented with 10% FBS (Gibco) plus 1% glutamine (Gibco). All culture growth media were supplemented with 10,000 U/mL penicillin–streptomycin (Gibco). HPDE-KRAS<sup>G12V</sup> cells were grown in RPMI supplemented with 10% FBS (Gibco) plus 1% glutamine (Gibco).

**Animal studies**

**Xenograft tumor experiments**

NOD.Cg-Prkdcscid Il2rgtm1Wjl/SzJ (NSG) mice were purchased from Jackson Laboratory and bred in the animal facility of CAST, G. D'Annunzio University, Chieti. Mice were housed on a 12-hour light/dark cycle and maintained at 24–26°C under pathogen-limiting conditions. Cages, bedding, and food were autoclaved before use, and food and water were provided *ad libitum*. Animal care and all experimental procedures were approved by the Ethics Committee for Animal Experimentation of the Institute according to Italian law (Authorization n°640/2022-PR). Seven-week-old mice were subcutaneously injected into the right flank with a suspension of 1.5 × 10<sup>6</sup> HPAF-II, KP-4, PaTu-8988t, and CAPAN-1 cells diluted in 200 µl of a 1:1 mixture of Matrigel (BD Biosciences) and PBS (Corning). Treatments were started when tumors reached palpable volumes. Decitabine, dissolved in saline, was administered intraperitoneally (IP) at 0.2 or 0.5 mg/kg body weight daily for the first week and three times a week for the following weeks. Olaparib, dissolved in 0.125% carboxymethylcellulose, was administered orally (OS) at 30 mg/kg body weight daily. Control mice received oral and IP treatments with vehicles only. Tumor volume was measured once or twice a week with calipers and calculated using the formula:  $V(\text{mm}^3) = L(\text{mm}) \times W(\text{mm})^2 / 2$ , where W is tumor width and L is tumor length. Mice were sacrificed when tumors in the control group reached 1 cm<sup>3</sup> in volume or were ulcerating, according to approved guidelines of the institution's animal ethics committee. The health status of the animals was monitored daily, and body weight was measured at least once a week during treatments, with the percentage of body weight loss calculated.

**METHOD DETAILS**

**Reagents and chemicals**

Decitabine (DEC), 5-Aza-2'-deoxycytidine (A3656), Dimethyl Sulfoxide (DMSO), Protease Inhibitor Cocktail, Bovine Serum Albumin, and β-Nicotinamide adenine dinucleotide (NAD<sup>+</sup>) No. N8410 were purchased from Sigma-Aldrich (St. Louis, MO, USA). Olaparib (OLA): AZD2281, Ku-0059436 (S1060), AZD1390, ATM Inhibitor (ATMi), and BAY-1895344, ATR Inhibitor (ATRI), were purchased from Selleckchem. Poly(ADP-ribose) Glycohydrolase (PARG) inhibitor: PDD00017273, was purchased from MedChemExpress. FxCycle™ PI/RNase Staining Solution was purchased from Thermo Fisher Scientific (Waltham, MA, USA). CellTiter-Glo Assay Reagent was purchased from Promega. Fetal Bovine Serum (FBS), Penicillin/Streptomycin (P/S), and 1% Glutamine were purchased from Gibco.

Antibodies are listed in each specific experimental section.

### KRAS dependency signature score calculation methods

Publicly available gene expression data for 41 pancreatic cell lines released by the CCLE Consortium<sup>41</sup> were analyzed. Gene signature scores were calculated by subtracting the average normalized expression of "down" genes from the average normalized expression of "up" genes, defining the L-score and the S-score. The microarray data were normalized by taking the log<sub>10</sub> ratio of expression of the sample compared to the average expression of the gene across all samples. The L-score genes are described in (8); the S-score genes are described in (9). The top KRAS-dependent genes were selected as "up" genes, and the top KRAS-independent genes were selected as "down" genes. The L and S scores of KRAS dependency do not correlate with the cellular proliferation index as estimated by the correlation analysis of the L and S scores with cellular doubling time (Figure S2).

### Cell viability assay and half-maximal inhibitory concentration (IC50) determination

The viability of cells was evaluated using the CellTiter-Glo Luminescent Cell Viability Assay (Promega). For KP-4, PaTu 8902, and PaTu 8988t, a total of  $5 \times 10^2$  cells were seeded at T=0. For CAPAN-1,  $1 \times 10^3$  cells were seeded onto 96-well plates. After 24 hours, cells were exposed to indicated serial concentrations of drugs, and culture media and treatments were refreshed after 72 hours. Viability was measured either 72 hours or 144 hours later, as indicated, using the CellTiter-Glo Luminescent Cell Viability Assay (Promega), according to the manufacturer's instructions. Dose-response curves and half-maximal inhibitory concentration (IC50) values with 95% CI were generated using GraphPad Prism software (GraphPad Software).

### Comet assay

#### Cell preparation

Cells ( $3000 \text{ cells/cm}^2$ ) were plated in 100mm dishes and treated after 24 hours as indicated. Cells were either used immediately or frozen in freezing medium in Eppendorf tubes and stored at  $-80^\circ\text{C}$ . When needed, cells were thawed at  $37^\circ\text{C}$ , centrifuged at  $4^\circ\text{C}$  for 10 minutes (1500 rpm), washed in 1x PBS, and centrifuged again. The cell suspension in 1x PBS ( $10 \mu\text{l}/50\text{k}$  cells) was combined with  $75 \mu\text{l}$  of 0.5% low melting point agarose (LMPA) at  $37^\circ\text{C}$ , gently mixed, and rapidly spread ( $75 \mu\text{l}$ ) onto a pre-coated glass slide with normal melting point agarose (NMPA). Slides were immediately covered with coverslips and the agarose was allowed to solidify at  $4^\circ\text{C}$  for about 5 minutes.

#### Alkaline comet assay

Coverslips were gently removed, and slides were immersed in alkaline lysis solution for at least 18-20 hours (no more than 5 days) at  $4^\circ\text{C}$  in the dark. Slides were then transferred into a horizontal electrophoresis tank containing freshly prepared electrophoresis buffer for 20 min at  $4^\circ\text{C}$  to allow DNA to unwind. Electrophoresis was performed at 0.6 V/cm (cm refers to the diagonal between the electrodes) and 250-300 mA for 20 minutes in the same alkaline solution. Slides were rinsed with Neutralization Buffer three times for 5 minutes each, washed with MilliQ-H<sub>2</sub>O, fixed with ice-cold 100% ethanol, and dried at room temperature in the dark.

#### Neutral comet assay

Coverslips were gently removed, and slides were immersed in freshly prepared neutral lysis solution for 45 minutes at  $4^\circ\text{C}$  in the dark. Slides were washed in 1x TBE at  $4^\circ\text{C}$  and transferred into a horizontal electrophoresis tank containing 1x TBE at  $4^\circ\text{C}$ . Electrophoresis was performed at 0.6 V/cm (cm refer to the diagonal between the electrodes) and 6-7 mA for 15 minutes. Slides were rinsed with MilliQ-H<sub>2</sub>O, fixed with ice-cold 100% ethanol, and dried at room temperature in the dark.

Slides were stained with Syber Safe diluted in MilliQ-H<sub>2</sub>O, and after at least 12 hours, observed for image acquisition using an Olympus AX70 microscope at 20x magnification. Images of at least 200 cells per sample were captured for analysis. Comet images were analyzed using Comet Score software to measure tail moment.

Statistical analyses were performed with GraphPad Prism 8 and R. For comparison between two groups, a Mann-Whitney test was performed for the p-value, and a Wilcoxon test was performed for the effect size. For comparisons between three or more groups, a Dunn test was performed for the p-value, and a Wilcoxon test was performed for the effect size.

### Solutions

- Alkaline Lysis Solution: 2.5 M NaCl, 100 mM EDTA, 10 mM Tris base, 4g NaOH (pH 10) in MilliQ-H<sub>2</sub>O. 1 hour before sample preparation, add 1% Triton X-100 and keep at  $4^\circ\text{C}$ .
- Electrophoresis Buffer: 30 ml 10N NaOH, 5 ml 200 mM autoclaved EDTA (pH 10), complete to 1L with dH<sub>2</sub>O and keep at  $4^\circ\text{C}$ .
- Neutralization Buffer: 0.4 M Tris-HCl (pH 7.5) in dH<sub>2</sub>O, autoclave, and keep at  $4^\circ\text{C}$ .
- Neutral Lysis Solution: 6 ml 0.5 M EDTA (pH 8), 5 ml 10% SDS, complete to 100 ml with MilliQ-H<sub>2</sub>O.
- TBE 10x: 108g Tris-base, 55g boric acid in 800 ml dH<sub>2</sub>O, add 40 ml 0.5 M EDTA (pH 8), adjust pH to 8.5 and complete to 1L, autoclave, and store at room temperature.

### Cell cycle analysis by flow cytometry

Cells were seeded in 100mm cell culture dishes. Twenty-four hours after plating, PaTu 8902 and PaTu 8988t were treated with DMSO (vehicle),  $0.025 \mu\text{M}$  5-aza-2'-deoxycytidine (Decitabine),  $1.37 \mu\text{M}$  Olaparib, or a combination of both drugs for 72 hours. HPAF-II cells were treated with DMSO (vehicle),  $0.045 \mu\text{M}$  Decitabine,  $1.4 \mu\text{M}$  Olaparib, or a combination of both drugs for 72 hours. CAPAN-1 and KP4 cells were treated with DMSO (vehicle),  $0.09 \mu\text{M}$  Decitabine,  $0.5 \mu\text{M}$  Olaparib, or a combination of both drugs for 72 hours. Approximately  $1 \times 10^6$  cells were harvested, washed in 1x PBS, fixed with cold 70% ethanol, and kept at  $-20^\circ\text{C}$  for 24 hours. Fixed

cells were re-suspended in FxCycle™ PI/RNase Staining Solution (Thermo Fisher Scientific) for 30 minutes before analysis by flow cytometry. Samples were acquired using either a FACScalibur Flow Cytometer (Becton Dickinson Company) or an Attune NxT Acoustic Focusing Cytometer (Thermo Fisher Scientific). The fcs files were analyzed using FlowJo software.

### Immunofluorescence analysis of DDR markers

Cells (3000 cells/cm<sup>2</sup>) were plated on glass coverslips in 24-well plates and treated after 24 hours with 1.25 μM DEC for the indicated time. Cells were washed twice with 1x PBS and fixed with 4% formaldehyde for 20 minutes at room temperature. Fixed cells were washed twice with 1x PBS and permeabilized using 0.25% Triton X-100/1x PBS solution for 5 minutes. After permeabilization, cells were washed three times with 1x PBS and then blocked with 1% bovine serum albumin (Sigma)/1x PBS solution for 40 minutes at room temperature. Cells were washed three times with 1x PBS and then incubated with primary antibody. After washing three times with 1x PBS, cells were incubated with secondary antibodies. After three more washes with 1x PBS, cells were mounted with Fluoroshield™ with DAPI (Sigma-Aldrich) and allowed to dry in the dark. After 24 hours, stained cells were acquired using an Olympus AX70 microscope at 40x or 60x magnification. For quantitative analysis, images were processed using CellProfiler, and nuclear foci were quantified in relation to the total number of cells. A custom pipeline in CellProfiler was developed to measure and export raw data containing both the total nuclei and foci per image, and the number of nuclear foci per cell. Parameters such as pixel unit diameter, threshold smoothing scale, and threshold correction factor were adjusted depending on the cell line. The number of foci per nucleus in treated cells was compared to that in control cells, with at least 50 cells per group used for statistical analysis with an unpaired t-test using GraphPad Prism 8 software. For confocal microscopy, primary antibodies were incubated one at a time, while secondary antibodies were incubated simultaneously. Imaging analysis was performed using a Leica SP5 confocal microscope.

Primary and Secondary Antibodies Used in Immunofluorescence Analysis are listed in the Key Resources Table.

### RAD51 score

Cells (1500 cells/cm<sup>2</sup>) were plated on glass coverslips in 24-well plates for 96 hours. Then, cells were washed two times with 1X PBS and fixed using 4% formaldehyde for 20 minutes at room temperature. Fixed cells were washed two times with 1X PBS and permeabilized using 0.25% Triton X-100/1X PBS solution for 5 minutes. After permeabilization, cells were washed three times with 1X PBS and then blocked using 1% bovine serum albumin (Sigma)/1X PBS solution for 40 minutes at room temperature. Cells were washed three times with 1X PBS and then incubated with RAD51 primary antibody (ab133534, Abcam, Cambridge, UK) at a 1:500 dilution in PBS-BSA (1%) for 2 hours at room temperature. The cells were then washed three times with 1X PBS and incubated with geminin-L-CE primary antibody (Leica Biosystems) for 1 hour. Next, cells were washed three times with 1X PBS and incubated with secondary antibodies (α-mouse, two drops/ml in PBS-BSA1% and α-rabbit, two drops/ml in PBS-BSA1%) for 1 hour at room temperature. After three washes with 1X PBS, cells were mounted with Fluoroshield™ with DAPI (Sigma Aldrich) and coverslips were then left to dry in the dark. After 24 hours, stained cells were acquired using an Olympus AX70 microscope at 40x or 60x magnification.

For automated geminin-positive cell and nuclear foci quantification, a custom pipeline in CellProfiler was developed to measure and export raw data containing both the geminin-positive nuclei per image and the number of nuclear foci per geminin-positive cell. The RescaleIntensity and MedianFilter modules relatively change the intensity range of each image and reduce noise. Then, total nuclei and geminin-positive nuclei are identified as primary objects and related with the RelateObjects module to determine the ratio between total nuclei and geminin-positive nuclei and classify them into two different groups with the ClassifyObjects module. The enhancement of speckles with the EnhanceOrSuppressFeatures module allows for the identification of RAD51 foci in all the cells. Lastly, the RelateObjects module was used to count the number of foci per geminin-positive cell. Parameters such as pixel unit diameter, threshold smoothing scale, and threshold correction factor change depending on the cell line.

Geminin-positive cells with at least three foci were considered HR proficient, and the percentage of HR proficient cells versus the total number of geminin-positive cells was considered the RAD51 score. Statistical analyses were performed using GraphPad Prism 8 with a Kruskal-Wallis test within RAD51 scores of the RAD51-low group and the RAD51-high group and a 2-way ANOVA test between the two groups.

### Genomic data analysis and microsatellite stability assessment

Genomic mutational profiles of the selected PDAC cell lines were analyzed using data from the COSMIC and cBioPortal databases. We specifically examined gene mutations and copy number alterations (CNAs) in genes associated with DNA damage response (DDR) and homologous recombination, which are known to influence OLA cytotoxicity. Microsatellite stability (MS) for each cell line was annotated using previous reports and analysis from the CCLE panel.<sup>42</sup>

### Subcellular protein fractions

Cells were washed in cold phosphate-buffered saline 1X (PBS1X) and then collected by scraping in phosphate-buffered saline 1X (PBS1X) containing 1X PIC (Protease inhibitor cocktail, Cat#P8340, Sigma-Aldrich, St. Louis, MO, USA). Cells were collected in Eppendorf tubes and centrifuged at 500xg at 4°C, the supernatant was removed, and the Nuclear Isolation Buffer (NIB) [15mM Tris-HCl pH 7.5, 60mM KCl, 15mM NaCl, 5mM MgCl<sub>2</sub>, 1mM CaCl<sub>2</sub>, 250mM Sucrose, 1mM DTT, 2mM NaV, 1X Protease Inhibitor Cocktail, 1X PMSF, 1mM PARGi, 0.1% NP-40] was added to the cell pellet and incubated on ice for 10 minutes. The resuspended pellets were centrifuged at 2000xg at 4°C for 5 minutes and the supernatant (Cytoplasmic fraction) was collected in a clean tube and frozen in dry

ice. The nuclei were gently washed twice with NIB buffer without detergent (NP-40) and then centrifuged at 2000xg for 5 minutes at 4°C. Nuclear Lysis Buffer (NLB) [20mM Tris-HCl pH 7.9, 300mM NaCl, 1.5mM MgCl<sub>2</sub>, 0.2mM EDTA, 0.5mM DTT, 1mM NaV, 1X Protease Inhibitor Cocktail, 1X PMSF, 1mM PARGi, 10% glycerol] was added to the pellet (nuclei) and incubated on ice for 30 minutes. After incubation, the supernatant (Nuclear Soluble fraction) was transferred to a clean tube and frozen in dry ice. NLB buffer complemented with 3 $\mu$ l/100 $\mu$ l of Micrococcal Nuclease and 5 $\mu$ l/100 $\mu$ l of CaCl<sub>2</sub> were added to the pellet, vortexed at maximum power for 15 seconds and incubated at 37°C for 5 minutes, then vortexed again and centrifuged at 16000xg for 10 minutes at 4°C. The obtained pellet was lysed with radioimmunoprecipitation assay buffer 1X (RIPA-1: 50 mM Tris-HCl [pH 7.8], 150 mM NaCl, 5 mM EDTA, 15 mM MgCl<sub>2</sub>, 1% Nonidet P-40, 0.5% sodium deoxycholate, 1 mM dithiothreitol, 1X protease inhibitors, 1X PMSF, 50mM NaF, 10 mM  $\beta$ -glycerophosphate and 1 mM Na<sub>3</sub>VO<sub>4</sub>), incubated on ice for 10 minutes, centrifuged at 14000xg for 10 minutes at 4°C, and then the supernatant (Nuclear Insoluble) was transferred to a clean tube and frozen in dry ice. The cleared protein extracts of every cell fraction were quantified using the Bradford method (Bio-Rad).

### Total cell lysates

Cells were washed in phosphate-buffered saline 1X (PBS1X) containing 1X protease inhibitor cocktail (Protease inhibitor cocktail, Cat#P8340, Sigma-Aldrich, St. Louis, MO, USA) and were lysed with a cell scraper in modified radioimmunoprecipitation assay buffer (RIPA-1: 50 mM Tris-HCl [pH 7.8], 150 mM NaCl, 5 mM EDTA, 15 mM MgCl<sub>2</sub>, 1% Nonidet P-40, 0.5% sodium deoxycholate, 1 mM dithiothreitol, 1X protease inhibitors, 1X PMSF, 50mM NaF, 10 mM  $\beta$ -glycerophosphate and 1 mM Na<sub>3</sub>VO<sub>4</sub>), and then immediately frozen in dry ice. Cleared protein extracts were obtained after sonication with Vibra-Cell™ Ultrasonic Liquid Processor VCX 500/VCX 750 (Sonics & Materials, Inc., Newtown, CT, USA) followed by centrifugation at 14000xg for 10 minutes at 4°C, and then the cleared protein extracts were quantified using the Bradford method (Bio-Rad).

### "Combenefit" method for drug combination index analysis

The sensitivity was tested in a 7-day-long proliferation assay. Cells were seeded in 96-well culture plates in different numbers per well depending on the cell line to reach 80%-90% confluency of control wells at the end of the assay. The following day, serial dilutions of Decitabine (1:4 for Pa-Tu-8902 and HPAF-II, 1:2 for Capan-1), and Olaparib (1:3 for Pa-Tu-8902 and HPAF-II, 1:2 for Capan-1), were added to the cells in single treatment and combining each concentration of the two drugs in a 4x5 matrix, then the treatments were refreshed after 72h. Seven days after the first treatment, the cell viability was assessed by Cell Titer-Glo Luminescent Cell Viability (CTG) assay (Promega) and measured by Varioscan Lux plate reader. Viability measured for each treatment condition was normalized to untreated controls. Final data are an average of at least three biological replicates with similar results. After CTG analysis, synergistic/antagonistic/additive combinations were analyzed using Combenefit software, which provides synergy distribution plots by comparing experimental data to mathematical models (e.g., HSA model) of dose responses for additive/independent combinations. The HSA model assesses the efficacy of a drug combination by comparing it to the effect of the single most effective drug in the combination. It operates under the assumption that the effect of the drug combination should not exceed the effect of the most potent single drug. In brief, the software first reads each experimental dose response as a matrix of percentages of the control and each single-agent effect is fitted with a dose-response curve. If the observed effect of the drug combination is greater than the effect predicted by the HSA model, the combination is considered synergistic. If the observed effect matches the predicted effect, the combination is considered additive. If the observed effect is less than the predicted effect, the combination is considered antagonistic. Combenefit applies the HSA model to the input data. The software calculates the expected effect of the combination based on the highest single-agent effect. The results are typically presented in a graphical format (e.g., heatmaps). Combenefit may also provide statistical metrics to quantify the degree of interaction, helping users to make more precise interpretations of the data.

### "Calculusyn" method for drug combination index analysis

Cells were treated with a combination of Ola and DEC using the method of constant ratio drug combination. The two drugs were used at a constant ratio of their concentrations. The concentrations used corresponded to 0.25, 0.5, 1, 2, and 4 times the IC<sub>50</sub> of each agent (Ola: IC<sub>50</sub>=5.5 $\mu$ M; DEC: IC<sub>50</sub>=100nM for Pa-Tu-8902, Ola: 7.8 $\mu$ M; DEC: IC<sub>50</sub>=180nM for HPAF-II, Ola: 1 $\mu$ M; DEC: IC<sub>50</sub>=90nM for Capan-1). This method, using the combination index (CI) equation, allows quantitative determinations of drug interactions at increasing levels of cell kill. The CI value allows classification of the anti-tumor activity of the drug combination: a CI of less than, equal to, or more than 1 indicates synergistic, additive, or antagonistic effects, respectively. Fa is the fraction of cell death induced by drug treatment and ranges from 0 to 1, with 0 meaning no cell killing and 1 representing 100% cell killing. The sensitivity was tested in a 7-day-long proliferation assay. Cells were seeded in 96-well culture plates in different numbers per well depending on the cell line to reach 80%-90% confluency of control wells at the end of the assay. After 24 hours, cells were treated with serial dilutions (1:2) of each drug alone or in combination at a constant ratio (Ola) in three independent experiments with triplicate samples, and the treatments were refreshed after 72h. Seven days after the first treatment, the cell viability was assessed by Cell Titer-Glo Luminescent Cell Viability (CTG) assay (Promega) and measured by Varioscan Lux plate reader. Viability measured for each treatment condition was normalized to untreated controls. Final data are an average of at least three biological replicates with similar results. To determine the nature (synergism, additivity, and antagonism) of Ola and DEC interaction, we used the method proposed by Chou and Talalay using the Compusyn software.

### Immunoblot analysis

Protein samples were separated on 4%–12% or 4%–20% Tris-Glycine gels (Novex™ WedgeWell™, Invitrogen, Waltham, MA, USA) and transferred to nitrocellulose membranes (Amersham™ Protran™ 0.45µm NC). Membranes were blocked in TBS-T (0.1% Tween-20) containing 5% bovine serum albumin, incubated with primary antibodies according to the manufacturer's instructions, and then incubated with horseradish peroxidase-conjugated goat anti-rabbit IgG (Cat#7074, Cell Signaling Technology, Inc., Danvers, MA, USA) or anti-mouse IgG (Bethyl Laboratories, A90-116P). Detection was performed using enhanced chemiluminescence (ECL SuperSignal™ West Femto Maximum Sensitivity Substrate, Thermo Scientific, Waltham, MA, USA). The following primary antibodies were used for Western blotting: PARP1 (46D11) Rabbit mAb (Cat#9532, Cell Signaling Technology, Inc.), PAR/pADPr Antibody (Cat#4335-MC-100, R&D Systems, Minneapolis, MN, USA), XRCC1 Antibody (Cat#2735, Cell Signaling Technology, Inc.), β-Actin antibody (No. SAB5600204, Sigma-Aldrich, St. Louis, MO, USA), Histone H3 (D1H2) XPR Rabbit mAb (Cat#4499, Cell Signaling Technology, Inc.), CHK1 (2G1D5) Mouse mAb (Cat#2360, Cell Signaling Technology, Inc.), phospho-RPA32 (S4/S8; Bethyl Laboratories, A300-245A), phospho-Chk1 (Ser345) (133D3) Rabbit mAb (Cat#2348, Cell Signaling Technology, Inc.), phospho-Chk1 (S317) (Cat#2344, Cell Signaling Technology, Inc.), phospho-Chk2 (Thr68) (Cat#2661, Cell Signaling Technology, Inc.), Chk2 (1C12) Mouse mAb (Cat#3440, Cell Signaling Technology, Inc.), phospho-Histone H2AX (Ser139) (Cat#05-636, Merck Millipore, Burlington, MA, USA), and RCC1 (N-19) (sc-1161, Santa Cruz Biotechnology, Inc., Santa Cruz, CA, USA). Statistical analyses were performed using GraphPad Prism 8 with a two-way ANOVA test for comparisons between pairs of cell lines, and one-way ANOVA with multiple comparisons through post-hoc Tukey HSD (Honestly Significant Difference) Test within each experimental set of cell lines. In the graph, the same letter represents no statistical relevance in the difference between groups, while different letters represent a  $p$ -value  $< 0.05$  for the difference between groups.

### Methods for human equivalent dose (HED) calculation

#### Decitabine posology

In clinical practice, decitabine (Dacogen®) is administered at a dose of 20 mg/m<sup>2</sup> body surface area via intravenous infusion over 1 hour, repeated daily for 5 consecutive days (i.e., a total of 5 doses per treatment cycle). The total daily dose must not exceed 20 mg/m<sup>2</sup>, and the cumulative dose per treatment cycle must not exceed 100 mg/m<sup>2</sup>. Treatment cycles are repeated every 4 weeks depending on the patient's clinical response and observed toxicity. Alternative posology schedules administering DACOGEN at a dose of 15 mg/m<sup>2</sup> by continuous intravenous infusion over 3 hours repeated every 8 hours for 3 days, or 10 mg/m<sup>2</sup> by continuous intravenous infusion over 1 hour repeated daily for d1-5 and d8-12 are also implemented in the clinical routine.

#### HED calculation

According to the Food and Drug Administration (FDA), the extrapolation of an animal dose to a human dose is most accurately performed through normalization to body surface area (BSA), typically represented as mg/m<sup>2</sup>.<sup>43</sup> The human equivalent dose (HED) can be calculated using the formula illustrated.<sup>43</sup>

To convert the dose used in mice to a human-equivalent dose based on BSA:

1. Multiply the mouse dose (0.2 mg/kg for DEC) by the Km factor for a mouse (Km = 3).
2. Divide the result by the Km factor for a human (Km = 37).

This calculation yields a human-equivalent dose of 0.016 mg/kg, which corresponds to 0.97 mg of DEC for a 60 kg individual.

To convert a dose from mg/kg to mg/m<sup>2</sup>, multiply by the Km value. This results in a human-equivalent dose of 0.6 mg/m<sup>2</sup> body surface area per day. This corresponds to a human-equivalent dose of 0.6 mg/m<sup>2</sup> body surface area per day, which is 15 to 30 times lower than the standard clinical dose used to treat human leukemia patients, as per the reference posology.

#### Olaparib posology

In clinical practice for adults, the standard dose of olaparib is 300 milligrams (mg) (two 150 mg tablets) taken twice daily, with each dose administered 12 hours apart. Physicians may adjust the dose as needed or based on patient tolerance; however, the total daily dose typically does not exceed 600 mg (four 150 mg tablets).

#### HED calculation

To calculate the human-equivalent dose (HED) for olaparib (OLA) based on doses used in mice, the body surface area (BSA) conversion method is applied.<sup>43</sup> Specifically:

1. Multiply the mouse dose (30 mg/kg for OLA) by the Km factor for a mouse (Km = 3).
2. Divide the result by the Km factor for a human (Km = 37).

This calculation yields a human-equivalent dose of 2.43 mg/kg, which corresponds to 146 mg of OLA for a 60 kg individual. The OLA doses used in the study, whether as a monotherapy or in combination treatments, were approximately 4-fold lower daily compared to standard clinical dosing in humans.

### Histological and immunohistochemical analysis

Primary tumors and lungs were fixed in 10% neutral buffered formalin, embedded in paraffin, and sectioned at a 5-µm thickness for histological analysis. To optimize the detection of microscopic metastases and ensure systematic uniform and random sampling,

lungs were cut transversally into 2.0-mm thick parallel slabs, with a random position of the first cut within the first 2 mm of the lung, resulting in 5-8 slabs per lung. The slabs were then embedded cut surface down and sections were stained with Hematoxylin and Eosin. Slides were independently evaluated by two pathologists to quantify the number of tumor lesions. Immunohistochemical staining on formalin-fixed paraffin-embedded (FFPE) tissue from tumor xenografts was performed using the following primary antibody: mouse monoclonal anti-pH2AX antibody (1/500 dilution; 05-636, Millipore). Antigen retrieval was performed by microwaving slides for 10 minutes in Tris-EDTA buffer (pH 9.0, Sigma Aldrich). After blocking for 10 minutes with protein block (Dako) at room temperature, sections were incubated for 30 minutes with anti-pH2AX. Envision anti-mouse IgG (Dako) was used as the secondary antibody for 30 minutes, followed by 3,3'-diaminobenzidine (DAB) as the chromogenic agent. After chromogen incubation, slides were counterstained in Hematoxylin (Bio-Optica) and images were scanned with a Nanozoomer scanner from Hamamatsu. Quantification of pH2AX (% of positive cells) was performed on whole tumor sections (5-6 samples per group) analyzed with QuPath 0.3.2 software using the positive cell detection tool. The percentage of positive cells was plotted using GraphPad Prism 5 software.

### QUANTIFICATION AND STATISTICAL ANALYSIS

The statistical details of experiments including the statistical tests used, the exact value of replicates (n) or the exact number of animals, number of cells, the definition of center, and dispersion and precision measures (e.g., mean, median, SD, SEM, confidence intervals) can be found in the figure legends, figures and, where appropriate, in the Results. All the in-vitro experiments were performed in triplicate wells and repeated multiple times using independent biological replicates (n). Student's t-test was used to test for statistical significance of differences between groups and controls. P values < 0.05 were considered statistically significant. Sample correlations were calculated using Spearman's correlation coefficient.

Statistical analysis for comet assays was performed using GraphPad Prism 8 and R. For comparison between two groups, a Mann-Whitney test was performed for the p-value and a Wilcoxon test was performed for the effect size. For comparisons among three or more groups, a Dunn test was performed for the p-value and a Wilcoxon test was performed for the effect size.

GraphPad Prism 8 was used for immunofluorescence nuclear foci quantification and group comparisons with an unpaired t-test. In the RAD51 score experiment, a Kruskal-Wallis test and two-way ANOVA were performed.

Statistical analyses for immunoblot analysis were performed using GraphPad Prism 8 and R with a two-way ANOVA test for comparisons between pairs of cell lines and one-way ANOVA with multiple comparisons through post-hoc Tukey HSD (Honestly Significant Difference) test within each experimental set of cell lines. In the graph, the same letter represents no statistical relevance in the difference between groups, while different letters represent a significant p-value (< 0.05) for the comparison between groups.

For xenograft-based model experiments, statistical differences between experimental groups were evaluated by applying a two-way ANOVA test or a two-tailed unpaired Student's t-test. Differences were considered statistically significant when p-values were less than 0.05. All analyses were conducted using GraphPad Prism 5 software (GraphPad, San Diego, CA, USA).